Insights into deglacial East Asian Monsoon seasonality and inter-regional teleconnections from Lake Suigetsu, Japan

Rex, C.L.[1,2], Staff, R.A.[1], Leng, M.J.[3], Toney, J.L.[2], Pearson, E.J.[4], Tyler, J.J.[5], Swann, G.E.A.[6], Lacey, J.H.[3], Saito-Kato, M.[7], Nakagawa, T.[8]

* Corresponding author (c.rex.1@research.gla.ac.uk)

1. Scottish Universities Environmental Research Centre (SUERC), University of Glasgow, Scottish Enterprise Technology Park, Rankine Avenue, East Kilbride, G75 0QF, United Kingdom
2. School of Geographical and Earth Sciences, University of Glasgow, Glasgow, G12 8QQ, United Kingdom
3. National Environmental Isotope Facility, British Geological Survey, Keyworth, NG12 5GG, UK
4. School of Geography, Politics and Sociology, Newcastle University, Newcastle upon Tyne, NE1 7RU, United Kingdom
5. Department of Earth Sciences, University of Adelaide, Adelaide, South Australia 5000, Australia
6. School of Geography, University of Nottingham, University Park, Nottingham, NG7 2RD, United Kingdom
7. Department of Geology and Paleontology, National Museum of Nature and Science, 4-1-1 Amakubo, Tsukuba-shi, Ibaraki Prefecture, 3050005, Japan
8. Research Centre for Palaeoclimatology, Ritsumeikan University, 1-chōme-1 Nojihigashi, Kusatsu, Shiga Prefecture, 525-0058, Japan

This is a preprint of an article that been submitted to Nature Communications, and revised based on one round of peer review at that journal, but has yet to be formally accepted for publication.

Abstract

The past evolution of the East Asian Monsoon (EAM) was affected by remote climate processes. However, there is uncertainty surrounding these teleconnections and their impact on each seasonal EAM mode during periods of rapid global change. Here we use the unique biannual precipitation patterns of central Japan to reconstruct winter and summer EAM evolution during the last glacial termination (22,000 – 10,000 cal BP). Oxygen isotope analysis of diatoms and hydrogen isotope analysis of n-alkanoic acids from the Lake Suigetsu sediment cores show that in Japan the winter EAM weakened and the summer EAM strengthened with deglaciation. Only the summer mode exhibited variations coeval with stade-interstade fluctuations. A relationship between the summer EAM and Antarctic temperature post-16,000 cal BP supports a remote link to the Southern Hemisphere. These trends were different to continental EAM records and highlight the value of broadening the geographical range of reconstructions to rationalise system heterogeneities.

Introduction

The East Asian Monsoon (EAM) region is located at a point of convergence of multiple, globally interconnected climatic systems, with the palaeo-EAM system demonstrably affected by remote surface and atmospheric processes on centennial to millennial timescales. This is most eminently exemplified by the teleconnection between summer EAM strength and North Atlantic temperature during the late Pleistocene; first evidenced by the relationship between the Hulu Cave stalagmite and Greenland ice core oxygen isotope ($\delta^{18}O$) records (Wang *et al.*, 2001; Zhang *et al.*, 2019) and subsequently corroborated by studies from across the region (Herzschuh, 2006; Liu *et al.*, 2022). This relationship is thought to have been driven by the influence of Atlantic Meridional Overturning Circulation (AMOC) on the position of the Intertropical Convergence Zone (ITCZ) (Zhang *et al.*, 2019). However, other reconstructions of EAM strength have noted an inverse relationship to Antarctic temperatures in this interval (Han *et al.*, 2016; Zhang *et al.*, 2016) and, as a result, the view

of teleconnections acting on the EAM region has expanded to consider links to other climate systems, including Antarctica and the Pacific Ocean.

The behaviour of the EAM during the last glacial termination (TI; 22,000 to 10,000 cal BP) is an ideal focus for characterising the changing seasonality of this system and the persistence of these teleconnections. As a global transition, TI exemplifies a substantial, detectable change in many palaeoclimate archives with the climate at the geographic poles (representing two possible "end member" teleconnection origins) decoupled, with a Southern Hemisphere lead (Denton *et al.*, 2010; WAIS Divide Project Members, 2013). In the North Atlantic, TI was characterised by colder conditions during Greenland Stade 2.1 (GS-2.1; ~22,900 to 14,700 cal BP) and Greenland Stade 1 (GS-1; ~12,800 to 11,700 cal BP), alternating with warmer conditions during Greenland Interstade 1 (GI-1; ~14,700 to 12,800 cal BP) and the Holocene (~11,700 cal BP onwards) (Rasmussen *et al.*, 2014). GS-2.1, GI-1 and GS-1 were equivalent to the Last Glacial Maximum (LGM), Bølling–Allerød (BA) Interstade and Younger Dryas (YD) Stade of the wider North Atlantic region. In the far Southern Hemisphere, warming was more gradual and interrupted only by the Antarctic Cold Reversal (ACR; 14,500 to 12,900 cal BP), which bestrode GI-1 and GS-1 (EPICA Community Members, 2006; WAIS Divide Project Members, 2013).

Whilst current evidence supports a weakening East Asian Winter Monsoon (EAWM) and strengthening East Asian Summer Monsoon (EASM) during TI on an orbital scale (Wang *et al.*, 1999; Gallagher *et al.*, 2018), centennial- to millennial-scale fluctuations in EAM strength and the relative seasonal contributions to annual precipitation are poorly constrained (particularly in the case of the EAWM; Wen *et al.*, 2016) and appear spatially heterogeneous (Zhang *et al.*, 2019). It is unsurprising, therefore, that there is uncertainty surrounding deglacial EAM evolution on submillennial timescales (Yoshida and Takeuti, 2009; Hayashi *et al.*, 2010; Liu *et al.*, 2022), particularly in terms of conflicting evidence for teleconnections to other regions. A possible source of this uncertainty is the limited number of available high-resolution EAM reconstructions. Consideration of both EAWM and

EASM strength in isolation is vital for deconvolving EAM behaviour during TI because they do not always show a perfectly inverse relationship (Wang *et al.*, 2012; Wen *et al.*, 2016; Yan *et al.*, 2020) and hence have the potential to exhibit unique behaviours (and teleconnection signals).

Due to its location, the EAM dominantly controls the climate of Japan; however, the relationship between the EAM and precipitation in Japan is unique. Japan is situated directly beneath the seasonally migrating monsoon front (Fig. 1), a critical geoclimatic boundary which moves northwards during summer and southwards during winter and separates the influence of the EAWM and EASM modes (Nakagawa *et al.*, 2006, Yoshida and Takeuti, 2009). The Japanese archipelago lies between two water bodies (the Pacific Ocean and the Sea of Japan), hence both EAM modes bring heavy precipitation to the country; mixed rainfall and snowfall concentrated along the Sea of Japan coast during the EAWM, and rainfall across the entire country during the EASM (Chowdary *et al.*, 2019; Amekawa *et al.*, 2021). This is in contrast to Continental Asia, where the EASM brings heavy rainfall from the Pacific Ocean, but the EAWM is predominantly dry because it originates inland (Yancheva *et al.*, 2007; Yan *et al.*, 2020). As such, the annual distribution of rainfall in Japan uniquely reflects a balance between both seasonal modes of the EAM. In light of these distinctive climatic characteristics, EAM records from Japan are well suited to deconvolve the complexities of EAM evolution during TI. In this study we present new stable isotope-based proxy records of both EAWM and EASM evolution in central Japan from the Lake Suigetsu sediment cores and compare these to a series of global benchmark records of EAM variability and temperature changes (Fig. 1), to better understand the factors affecting both seasonal modes of the EAM in Japan during this interval.

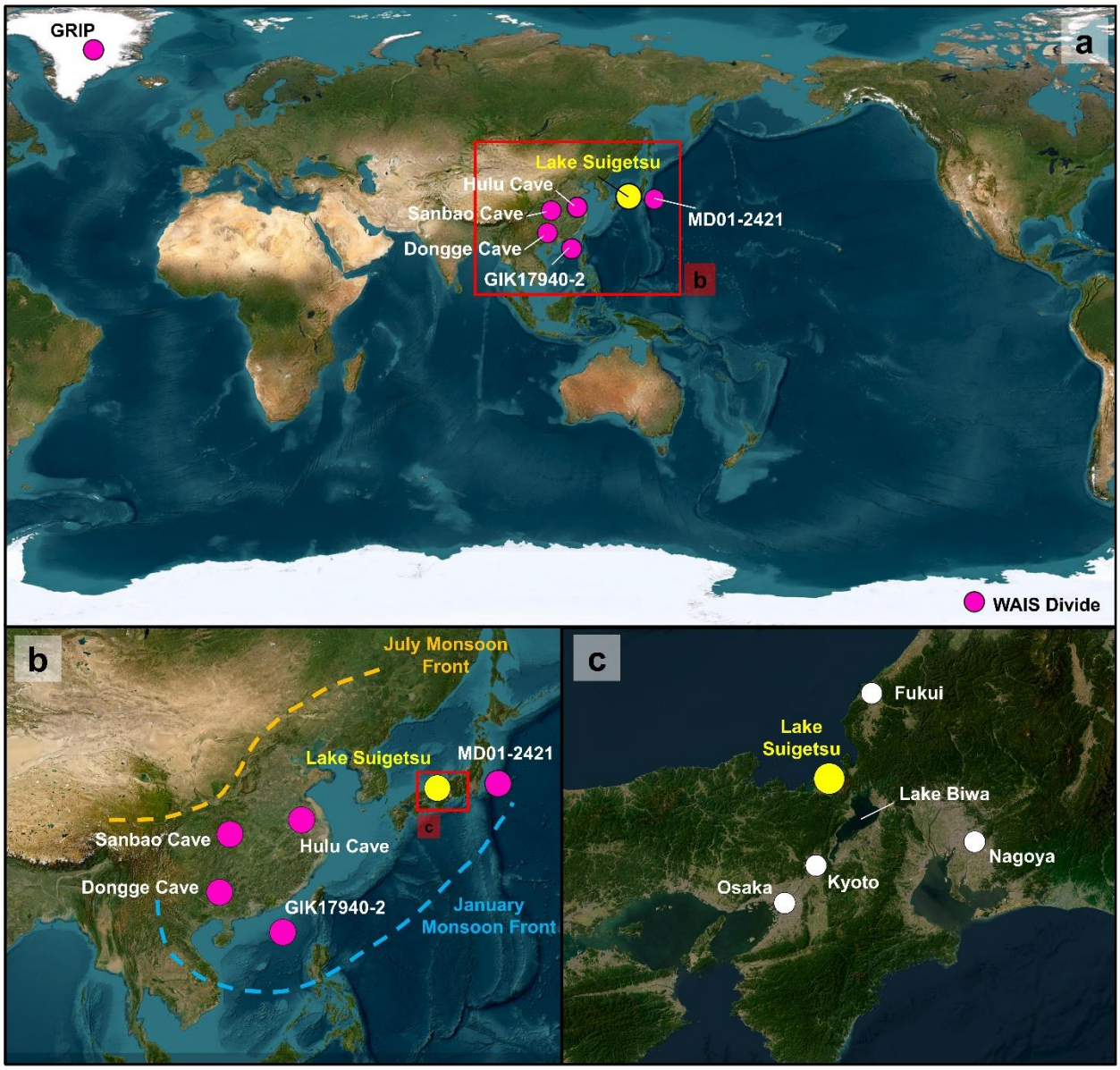

Fig. 1 – Lake Suigetsu and other key sites. a) the key global benchmark record sites discussed in the main text. b) the sites within the EAM region, alongside the average positions of the modern monsoon front in January and July (adapted from Nakagawa *et al.*, 2006). c) the location of Lake Suigetsu in Fukui Prefecture, central Honshu, relative to key cities and geographical features in Japan. Red boxes show the extent of subsequent panels in the sequence. Basemap is World Imagery (WGS84) from Esri (2023) (scale 1:37,314,123 (a), 1:7,851,046 (b), 1:530,430 (c)).

Lake Suigetsu is a tectonic lake located ~1 km from the Sea of Japan in Fukui Prefecture, Honshu Island (35˚ 35’ N, 135˚ 53’ E; Fig. 1; Nakagawa *et al.*, 2012). Suigetsu was a freshwater lake for the last glacial-interglacial cycle, except during global sea level highstands in the Eemian and the mid-Holocene, and post-1664 CE when the lake was artificially connected to the Sea of Japan (Nakagawa *et al.*, 2021). Four previous deep coring campaigns carried out in 1993 (SG93 core), 2006

(SG06), 2012 (SG12) and 2014 (SG14) recovered a series of overlapping sediment core sections from the present day to >150,000 yr BP (Nakagawa *et al.*, 2012). The preserved sequence, covering >98 m of composite sediment depth, provides a palaeoenvironmental archive that captures two glacial and two full interglacial periods of continuous sedimentation. The Suigetsu cores contain annual laminations (varves) between ~70,000 yr BP and 10,000 cal BP, and between ~50,000 and 10,000 cal BP comprise the longest continuously varve-counted record from the Quaternary (Schlolaut *et al.*, 2018). Thin-section microscopic analysis showed that the varves comprise a spring layer of *Aulacoseira* diatoms with some siderite, a detrital layer containing silt-sized quartz and feldspar, a summer layer of light amorphous organic material, an autumn layer of *Encyonema* diatoms within siderite, and a transitional autumn-to-winter clay layer (Schlolaut *et al.*, 2012).

Previous studies of the Suigetsu sediments from TI substantiate that this was a period of significant climatic change at the catchment. Pollen-derived temperature reconstructions of this interval show a structure which resembles that of North Atlantic temperature: abrupt warming at the start of a “Late Glacial Interstade”, a more gradual decrease in temperature into a “Late Glacial Stade”, and an abrupt warming at the start of the Holocene (Nakagawa *et al.*, 2021). However, whilst the onset of the Late Glacial Stade and the Holocene at Lake Suigetsu were synchronous with the Younger Dryas and Holocene periods in the North Atlantic, the Late Glacial Interstade at Lake Suigetsu commenced ~200 years prior to its North Atlantic counterpart (the Bølling–Allerød) (Nakagawa *et al.*, 2021). This behaviour was rationalised by a sudden repositioning of the westerly jet to the north of the Himalayas (a topographical barrier which causes bimodality in the positioning of the jet) during boreal summer, which allowed warm air from the Pacific Ocean to propagate northwards and caused the step-change in summer temperatures in Japan. Conversely, it was an AMOC switch-on ~200 years later (due to a higher threshold response to insolation forcing), which resulted in a shift to interstadial conditions in the North Atlantic. On a subcentennial scale, multiproxy analysis of the Suigetsu cores showed a bipartite structure to the Late Glacial Stade with

a transition that was synchronous, albeit slower and more muted, to those observed at Lakes Meerfelder Maar (Germany) and Kråkenes (Norway) (Schlolaut *et al.*, 2017). A shift from *Aulacoseira ambigua* to *Aulacoseira subarctica* dominance during deglaciation was attributed to variations in the EAWM, affecting vegetation coverage and the water nutrient status (Kossler *et al.*, 2011). Carbon and nitrogen isotope ratios from chlorins also suggest an increase in aquatic primary productivity from glacial to interglacial conditions in the lake (Tyler *et al.*, 2010).

Here we present EAM precipitation reconstructions from Lake Suigetsu based on two proxy systems: the oxygen isotope composition of aquatic diatom silica frustules ($\delta^{18}O_{diatom}$) and the compound-specific hydrogen isotope composition of n-alkanoic acids ($\delta^{2}H_{acid}$) produced by aquatic algae (C_{16} and C_{18} homologues) and terrestrial plants (C_{28} and C_{30} homologues). Analysis was conducted using 100-year contiguous (continuous adjacent) samples. These proxies were selected based on target material abundances in the Lake Suigetsu cores and the ability to reconstruct both autochthonous (aquatic; $\delta^{18}O_{diatom}$, $\delta^{2}H_{C16acid}$ and $\delta^{2}H_{C18acid}$) and allochthonous (terrestrial; $\delta^{2}H_{C28acid}$ and $\delta^{2}H_{C30acid}$) changes during TI (Leng and Barker, 2006; Holtvoeth *et al.*, 2019). Both isotope proxy systems are versatile tools in palaeolimnological reconstructions of climate and follow the principle that the isotope composition of palaeo-catchment water was incorporated (via biosynthetic processes) into target materials by diatoms, algae, and plants, and preserved in the lake (Leng and Barker, 2006; Holtvoeth *et al.*, 2019). $\delta^{18}O_{diatom}$ and $\delta^{2}H_{acid}$ can be affected by fractionation processes during the life cycle of their respective source organisms but are dominantly controlled by the isotope composition of their water source (Leng and Marshall, 2004; Holtvoeth *et al.*, 2019). Hence, broader-scale palaeohydrological inferences can be made, relating to regional-scale shifts in atmospheric circulation and water vapour transport (Leng and Marshall, 2004; García-Alix *et al.*, 2021; Tierney *et al.*, 2022). At Lake Suigetsu, the modern isotope composition of water within the catchment is closely related to that of precipitation (with minimal effects of evaporation in summer), which is dominantly controlled by both the EAWM and EASM (Rex *et al.*, 2023, preprint), supporting

159 the utilisation of $\delta^{18}O_{diatom}$ and $\delta^{2}H_{acid}$ for reconstructing past EAM behaviour. Other potential
160 influencing factors are water temperature in the aquatic domain, and air temperature and
161 vegetation changes in the terrestrial domain (Leng and Barker, 2006; Castañeda and Schouten, 2011;
162 Sachse *et al.*, 2012).
163
164 **Results**
165 ***Observations at Lake Suigetsu***

166 The $\delta^{18}O_{diatom}$ values increased smoothly during TI with no abrupt shifts and the Holocene
167 values were ~2.5 ‰ higher than in the LGM (Fig. 2a). Key features of this profile were high frequency
168 centennial-scale fluctuations and higher values between 22,000 and 21,000 cal BP. The $\delta^{2}H_{C16acid}$
169 values followed a smooth trend to lower values through the record, except from 22,000 – 21,000
170 cal BP (when low values were observed), 19,000 – 17,000 cal BP (when values fluctuated drastically
171 on a centennial scale), and sections of the Late Glacial Interstade and Late Glacial Stade (when this
172 proxy exhibited periods of lower-than-average values; Fig. 2b). The difference between the $\delta^{2}H_{C16acid}$
173 values at 21,000 cal BP and 10,000 cal BP was ~50 ‰. The $\delta^{2}H_{C18acid}$ profile resembled that of
174 $\delta^{2}H_{C16acid}$, however long-term trends were harder to identify due to limited data coverage (see
175 Methods) and rapid high-amplitude fluctuations (Fig. 2c). Many of these coincided with equivalent,
176 lower amplitude, variations in the $\delta^{2}H_{C16acid}$ values, suggesting that these were closely related. The
177 $\delta^{2}H_{C28acid}$ and $\delta^{2}H_{C30acid}$ profiles also showed very similar behaviour to one another; decreasing
178 through the LGM and into the Late Glacial Interstade before initially increasing smoothly for ~2000
179 years, and then decreasing from the early Holocene onwards (Fig. 2d. Fig. 2e). Like the other $\delta^{2}H_{acid}$
180 proxies, the $\delta^{2}H_{C28acid}$ and $\delta^{2}H_{C30acid}$ records showed a period of lower values between 22,000 and
181 21,000 cal BP before a marked shift at 21,000 cal BP to higher values. The difference between the
182 $\delta^{2}H_{C30acid}$ values at 21,000 cal BP and 10,000 cal BP was ~35 ‰. The $\delta^{2}H_{C28acid}$ and $\delta^{2}H_{C30acid}$ profiles

were only decoupled between 19,000 and 17,000 cal BP; within this section both proxies showed rapid high amplitude changes which were offset by as little as one sample (100 years).

It appears that the shortest (C_{16}) and longest (C_{30}) chain lengths exhibited δ^2H_{acid} profiles with the most unique trends and the most complete data coverage, and hence we focus on these in subsequent discussions, whereas the $\delta^2H_{C18acid}$ values were limited in quantity and the $\delta^2H_{C28acid}$ values showed some features similar to the $\delta^2H_{C18acid}$ profile, possibly due to C_{28} n-alkanoic acids originating from a combination of aquatic and terrestrial sources. Whilst C_{30} n-alkanoic acids originate from strictly terrestrial sources, C_{28} n-alkanoic acids have been known to originate from aquatic and terrestrial sources (van Bree *et al.*, 2018; Tierney *et al.*, 2022). None of the trends exhibited by the isotope proxies resembled those of the pollen-derived temperature reconstructions at Lake Suigetsu (mean temperature of the warmest month, MTWA or mean temperature of the coldest month, MTCO; Fig. 2f, Fig. 2g; Nakagawa *et al.*, 2021). Proxies reflective of local catchment change (e.g., total organic carbon, n-alkanoic acid concentrations and diatom frustule concentration) exhibited smooth fluctuations during TI (Supplementary Fig. 1). Of these, only diatom frustule concentration showed any step-changes (at the onset of the Late Glacial Interstade), suggesting that the other proxies were driven by gradual changes, as for the $\delta^{18}O_{diatom}$ and δ^2H_{acid} values (Supplementary Discussion 1).

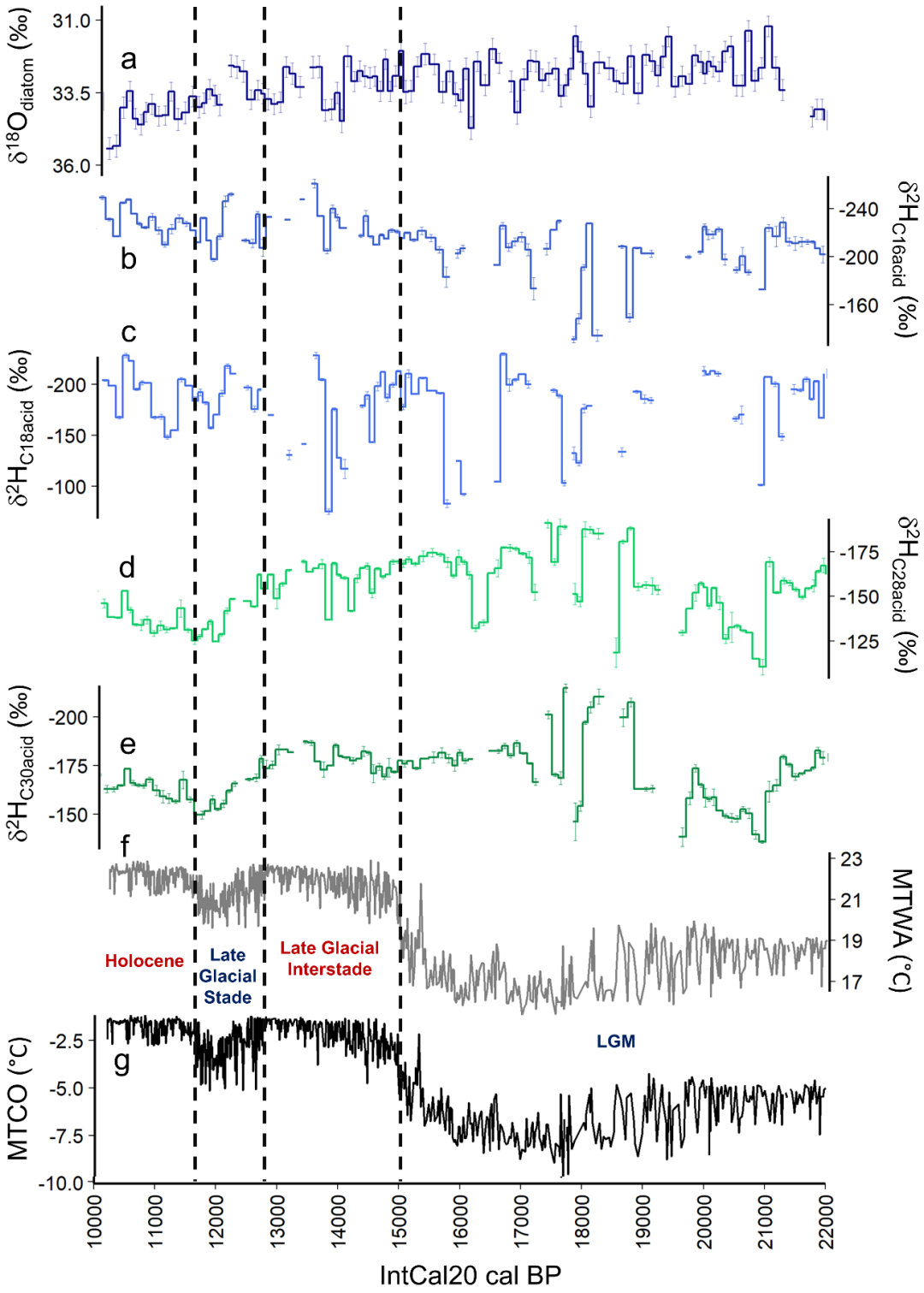

Fig. 2 – Proxy changes at Lake Suigetsu during Termination I. a) $\delta^{18}O_{diatom}$ (this study), b) $\delta^{2}H_{acid}$ of C_{16} n-alkanoic acids (this study), c) $\delta^{2}H_{acid}$ of C_{18} n-alkanoic acids (this study), d) $\delta^{2}H_{acid}$ of C_{28} n-alkanoic acids (this study), e) $\delta^{2}H_{acid}$ of C_{30} n-alkanoic acids (this study), f) MTWA; mean temperature of the warmest month (pollen-derived; Nakagawa *et al.*, 2021), g) MTCO; mean temperature of the coldest month (pollen-derived; Nakagawa *et al.*, 2021). Panels A to E are displayed inverted, and show data derived from 100-year integrated contiguous samples. All panels are on the IntCal20 timescale. Vertical dashed lines indicate the phases of temperature change at Suigetsu as designated by the pollen-derived temperature reconstructions (Nakagawa *et al.*, 2021).

Proxy Drivers

Determination of the dominant isotope proxy drivers is critical for interpreting the results in the context of EAM behaviour. Whilst multiple factors can affect the proxy values presented here, valuable insights can be made by identifying the dominant driver (which can cause the largest amplitude changes) in each case. There was no identifiable relationship between our isotope proxy values and the pollen-derived temperature or the primary pollen taxa concentrations, which eliminates air temperature (and thus water temperature) and vegetative change as the main drivers, respectively. There is a temperature dependent fractionation on $\delta^{18}O_{diatom}$ in precipitation and a mineral-water fractionation, which have opposing effects, but the impact is likely to be small. Given the amount of variation, we suggest that changes in water source composition were most likely the dominant control on the $\delta^{18}O_{diatom}$ and $\delta^{2}H_{acid}$ values. The isotope composition of modern catchment waters is principally governed by the composition of EAM-borne precipitation, as shown by extended monitoring (Rex *et al.*, 2023, preprint). EAM precipitation composition is determined by a combination of source composition and transport processes; in general, a "stronger" EAM, associated with strong winds and large quantities of precipitation integrated across the transport pathway, would act to lower $\delta_{precipitation}$, and the reverse qualities (for a "weaker" EAM) would provide higher $\delta_{precipitation}$ values (Yuan *et al.*, 2004; Zhang *et al.*, 2018). EAM strength is ultimately driven by an enhanced land-sea pressure gradient, moisture availability and conditions favourable for evaporation at source (Mohtadi *et al.*, 2016). It follows that these were the critical drivers of the isotope proxy systems during TI. On shorter timescales, other influences (e.g., local summer evaporation) could have also affected the isotope proxies, although there is a limited influence of evaporation on catchment isotopes in the modern day (Rex *et al.*, 2023, preprint), so we expect these to have caused small-amplitude effects, if any. The marked seasonality of EAM precipitation at Lake Suigetsu, combined with the short residence time of the lake (on the order of a few months; Rex *et al.*, 2023, preprint) means that isotope proxy seasonality is crucial for attribution to one or

both seasonal EAM modes. A key element of this designation is related to the modern catchment transit lag of approximately three months (Rex *et al.*, 2023, preprint), which signifies that surface lake water isotope composition (δ_{lake}) reflects that of the precipitation ($\delta_{precipitation}$) delivered in the preceding season, i.e., spring δ_{lake} is equivalent to that of winter $\delta_{precipitation}$ and so on. Consistently, deep water δ_{lake} is homogeneous and reflects annually integrated $\delta_{precipitation}$.

In a palaeo context, different diatom taxa were associated with each of the predominant seasonal blooms in the lake (spring and autumn) and consequently, the $\delta^{18}O_{diatom}$ values reflect a combination of seasonal signals. Of the most abundant diatom taxa, mixed planktonic *Aulacoseira subarctica* and *Aulacoseira ambigua* diatoms bloomed in the spring and captured surficial spring $\delta^{18}O_{lake}$ (winter $\delta^{18}O_{precipitation}$), and benthic *Encyonema* diatoms bloomed during the autumn and captured annually integrated $\delta^{18}O_{precipitation}$ from the homogenous deep water (bloom season attributions were derived from the varve structure; Schlolaut *et al.*, 2012). The signals captured by other taxa would have been dependent on their habitation depths and bloom seasons, however due to their low abundance relative to *Aulacoseira* and *Encyonema* diatoms, their seasonality was not ascribed as part of the varve structure. "Bulk" $\delta^{18}O_{diatom}$ therefore reflects mixed seasonality, with the relative weighting of each seasonal signal dependent on the mass contribution of each taxon (Leng and Barker, 2006). In the absence of quantified taxa-specific masses within each sample, the abundance (based on frustule counts) of each taxon can be used to provide an indication of the relative seasonal weighting of the $\delta^{18}O_{diatom}$ values; differences in taxon size can introduce uncertainty to this process, but we believe this to be a reasonable assessment because whilst other taxa are larger in size, the smallest genus of diatom, *Aulacoseira,* has thick valves and hence contributes significantly to the total diatom mass. Due to its relationship with winter $\delta^{18}O_{precipitation}$, *Aulacoseira* $\delta^{18}O_{diatom}$ offers the most robust links to EAWM behaviour. In theory, this connection may have been affected by alterations to the transit lag, however we believe that the relationship was maintained throughout TI, despite climatic variability, because the spring diatom bloom in Lake

Suigetsu is closely related to the delivery of the bulk of winter precipitation to the lake (i.e., both are caused by snow and ice melting). Additionally, winter is the wettest season of the year, minimising the effect of the preceding autumnal precipitation on the composition of surface δ_{lake} (an effect amplified by the short residence time of the lake). In light of this, it is reasonable to utilise the $\delta^{18}O_{diatom}$ values as an indicator of EAWM behaviour (i.e., strongly weighted towards winter $\delta^{18}O_{precipitation}$), when *Aulacoseira* was the most abundant genus. This was the case for earlier parts of the interval (22,000 – 19,800 cal BP) and from 15,000 cal BP onwards, when %*Aulacoseira* (*Aulacoseira* frustules as a percentage of total diatom frustules) was consistently greater than 60 % (and often greater than 70 %) on a centennial basis (Supplementary Fig. 2). This was likely to have been even greater in our $\delta^{18}O_{diatom}$ samples, which contained only diatoms which were smaller than 80 µm, favouring the (smaller) *Aulacoseira* over other taxa. However, the presence of other taxa may have contributed to the low amplitude centennial-scale variability in the $\delta^{18}O_{diatom}$ record throughout, and had greater influence between 19,800 and 15,000 cal BP. Maturation effects (i.e., post-mortem isotope exchange) remain an unconstrained influence on $\delta^{18}O_{diatom}$ (e.g., van Hardenbroek *et al.*, 2018), however (as with other studies) we do not expect this to be a dominant driver because the hydrous (most readily exchangeable) layer of each diatom was removed prior to measurement (see Methods) and only the more resistant structurally bound oxygen fixed during early sedimentation was analysed.

The $\delta^{2}H_{acid}$ values are associated with less complex seasonality than the $\delta^{18}O_{diatom}$ values, because the growth of terrestrial plants occurs predominantly during spring and summer (Sachse *et al.*, 2012) and lake-based organic matter production in Lake Suigetsu occurs almost exclusively in summer when the lake becomes stratified and aquatic productivity is high (Schlolaut *et al.*, 2012). Indeed, because the terrestrial $\delta^{2}H_{acid}$ values would have been unaffected by the catchment transit lag (the source water of terrestrial plants being soil pore water not lake water), we expect the $\delta^{2}H_{C30acid}$ values to have been heavily weighted towards summer (EASM) $\delta^{2}H_{precipitation}$. However, not

only would the aquatic δ^2H_{acid} values have been affected by the transit lag (and hence captured the isotope composition of spring $\delta^2H_{precipitation}$ = summer δ^2H_{lake}), but during periods of cold winters (which TI typifies), we might expect extension of the transit lag time in the first half of the year due to greater longevity of snow on the surrounding hillsides and hence slower delivery of precipitation to the lake system (Rex *et al.*, 2023, preprint). As a result, both winter and summer precipitation would enter the lake in quicker succession. Under these circumstances, summer δ^2H_{lake} would have become a greater seasonal mix of EAWM $\delta^2H_{precipitation}$ (entering the lake in late spring) and EASM $\delta^2H_{precipitation}$ (entering the lake in late summer). Consequently, the $\delta^2H_{C16acid}$ values reflect the weighted average of annual $\delta^2H_{precipitation}$. By calculating the numerical difference between the $\delta^2H_{C16acid}$ and $\delta^2H_{C30acid}$ values, it is possible to qualitatively infer the relative influence of the EAWM and EASM on the lake through time (Supplementary Discussion 2, Supplementary Fig. 3), although there is also an effect of reduced lag time with warming on this signal.

EAM Behaviour in Japan During TI

By considering the high *%Aulacoseira* intervals in isolation (Supplementary Fig. 2), variations in the $\delta^{18}O_{diatom}$ values strongly support a reduction in EAWM strength during TI in Japan (Fig. 3d). This aligns with Japanese stalagmite reconstructions of EAWM behaviour from the LGM and Holocene (Sone *et al.*, 2013; Amekawa *et al.*, 2021). It is possible that EAWM weakening caused higher $\delta^{18}O_{diatom}$ values both directly (as discussed above) and indirectly (by reducing EAWM surface runoff into the Sea of Japan, resulting in a transition from low- to high-salinity conditions in these EAWM source waters (Amekawa *et al.*, 2021)). The $\delta^{18}O_{diatom}$ profile does not exhibit stade-interstade-like fluctuations as seen in the North Atlantic (typified by GRIP $\delta^{18}O_{ice}$; Fig. 3a; Rasmussen *et al.*, 2014) or Antarctica (typified by WAIS Divide $\delta^{18}O_{ice}$; Fig. 3h; WAIS Divide Project Members, 2013), refuting the dominance of any such teleconnection between these regions and the EAWM during TI. Indeed, the $\delta^{18}O_{diatom}$ record does not show long term trends which parallel any of the

benchmark records shown in Fig. 3 suggesting that, instead, EAWM weakening during TI followed a more gradual trend akin to Northern Hemisphere summer insolation (albeit inversely; Fig. 3j; Laskar *et al.*, 2004). The trend in the $\delta^{18}O_{diatom}$ values between 22,000 and 21,000 cal BP inversely aligns with sea surface temperature (SST) records from the Northwest Pacific (Fig. 3i; Oba and Murayama, 2004; Oba *et al.*, 2006), suggesting that EAWM strengthening during this 1000-year interval was due to the intensification of glacial conditions in the region.

Variations in the $\delta^{2}H_{C30acid}$ values support an overall strengthening of the EASM in Japan during TI (with lower values in the Holocene than the LGM), however this was non-linear and occurred in three phases: EASM strengthening from the LGM into the Late Glacial Interstade, EASM weakening from the Late Glacial Interstade to the early Holocene, and subsequent EASM strengthening (Fig. 3f). An overall increase of EASM strength in Japan is also sustained by grain size variations within the South China Sea core GIK17940-2 (<63 µm fraction; Fig. 3g; Wang *et al.*, 1999); although the trend at Lake Suigetsu is not entirely equivalent to this because the South China Sea record shows a gradual, rather than tripartite, increase in EASM strength. Our reconstruction indicates that EASM behaviour in Japan was also characteristically different to EASM behaviour in Continental Asia (Chinese cave composite $\delta^{18}O_{speleothem}$; Fig. 3b; Cheng *et al.*, 2016) and did not show a response to North Atlantic-style stade-interstade fluctuations (Fig. 3a; Rasmussen *et al.*, 2014). However, a close inverse relationship is observed between EASM strength in Japan and Antarctic temperatures (illustrated by WAIS Divide $\delta^{18}O_{ice}$, Fig. 3h; WAIS Divide Project Members, 2013) between 16,000 and 10,000 cal BP, including coincident timing of inflections at ~14,500 cal BP, ~13,000 cal BP and ~12,000 cal BP (i.e., a response to the ACR). This provides compelling evidence for a teleconnection between the polar southern hemisphere and the EASM during this interval. Prior to this, the $\delta^{2}H_{C30acid}$ values were decoupled from WAIS Divide $\delta^{18}O_{ice}$, suggesting that this teleconnection was only activated at this time. During the LGM, the $\delta^{2}H_{C30acid}$ profile was distinctive and showed large amplitude fluctuations which did not occur synchronously with changes in the

global benchmark records, but many of these were also observed in the $\delta^2H_{C16acid}$ values. Interpretation of this time period is complex and is presented in the Discussion section below.

The $\delta^2H_{C16acid}$ values display a composite trend (Fig. 3e) which encapsulates characteristics of both the $\delta^{18}O_{diatom}$ (Fig. 3d) and $\delta^2H_{C30acid}$ (Fig. 3f) records. The influence of each of these unique behaviours appears to dominate the $\delta^2H_{C16acid}$ values at different times during the interval: similarities between the $\delta^2H_{C16acid}$ and $\delta^2H_{C30acid}$ profiles are observed during the early part of the ACR and the Holocene; in the latter stages of the ACR the $\delta^2H_{C16acid}$ profile resembles that of $\delta^{18}O_{diatom}$; and prior to 17,000 cal BP the $\delta^2H_{C16acid}$ profile shows mixed behaviour. These observations are consistent with our assertions that the $\delta^2H_{C16acid}$ values reflect a combined EAWM and EASM signal, weighted to the season with a greater quantity of precipitation, and these results support a changing balance between EAWM and EASM dominance in Japan during TI. The $\delta^2H_{C16acid}$ values show more EAWM character during the later stages of the ACR, when the EAWM was strong and EASM strength was declining, but shows greater EASM affinity during the early ACR and the Holocene, when there was a strengthened EASM and a weakened EAWM. The numerical difference between the $\delta^2H_{C16acid}$ and $\delta^2H_{C30acid}$ values suggests an increasing EASM influence on Lake Suigetsu through time (Supplementary Fig. 3) which is consistent with our independent observations of EAWM and EASM strength from the $\delta^{18}O_{diatom}$ and $\delta^2H_{C30acid}$ values.

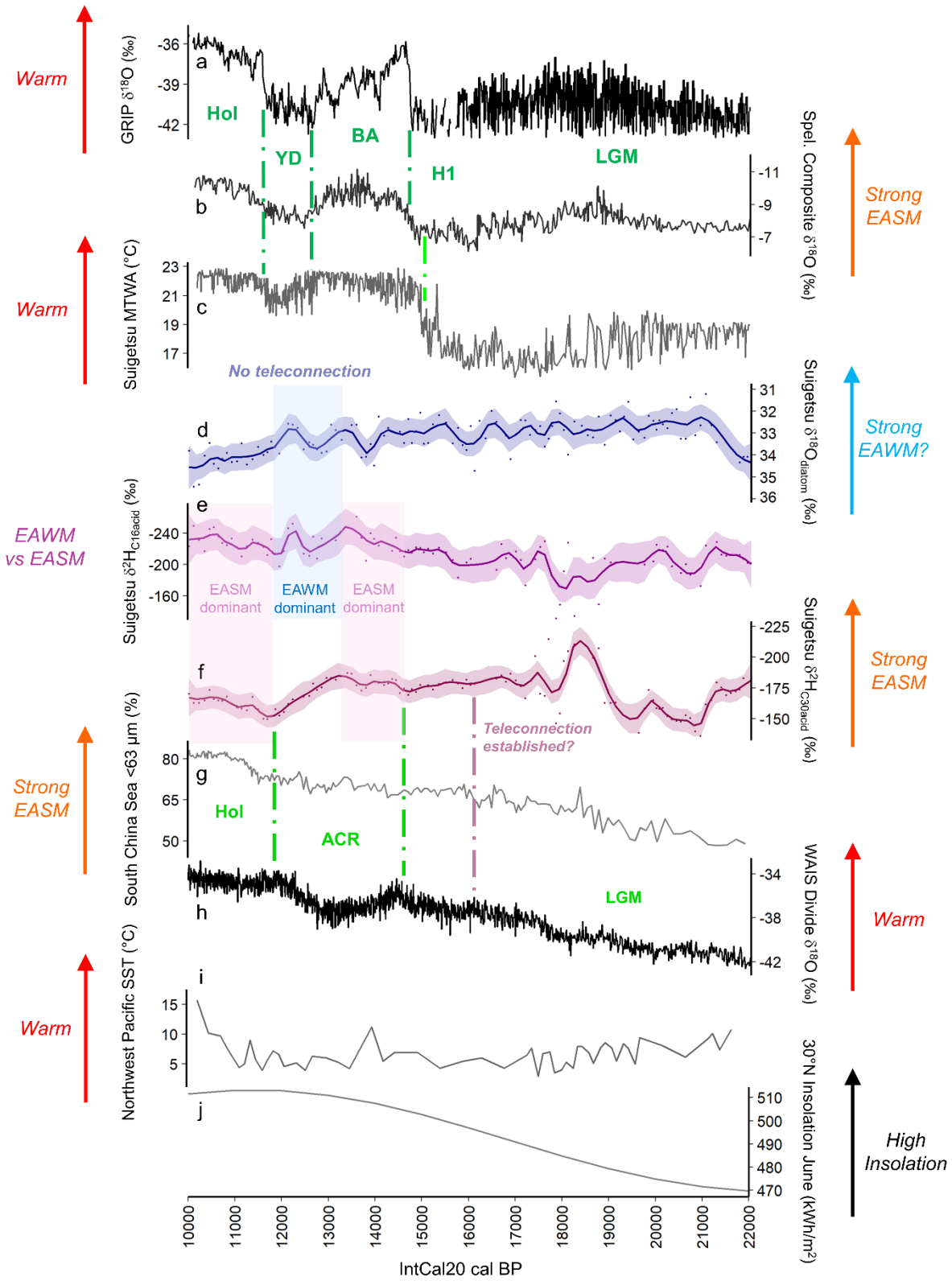

351

352 **Fig. 3 – EAM evolution at Lake Suigetsu during Termination I with contextual global benchmark records.** a) GRIP $\delta^{18}O_{ice}$
353 (Johnsen *et al.*, 1997; Rasmussen *et al.*, 2014; remodelled onto U-Th timescale), b) Chinese Cave Composite (Hulu,
354 Dongge, Sanbao) $\delta^{18}O_{speleothem}$ (Cheng *et al.*, 2016; U-Th timescale), c) Lake Suigetsu MTWA; mean temperature of the
355 warmest month (pollen-derived; Nakagawa *et al.*, 2021; IntCal20 timescale), d) Lake Suigetsu $\delta^{18}O_{diatom}$, loess smoothed
356 (span = 0.1) with 1σ confidence bands (this study; IntCal20 timescale), e) $\delta^{2}H_{acid}$ for C_{16} n-alkanoic acids, loess smoothed
357 (span = 0.1) with 1σ confidence bands (this study; IntCal20 timescale), f) $\delta^{2}H_{acid}$ for C_{30} n-alkanoic acids, loess smoothed
358 (span = 0.1) with 1σ confidence bands (this study; IntCal20 timescale), g) South China Sea (GIK17940-2) grain size

proportion <63 µm (Wang *et al.*, 1999; remodelled on to IntCal20 timescale), h) WAIS $\delta^{18}O_{ice}$ (WAIS Divide Project Members, 2013; WD2014 timescale), i) Northwest Pacific (MD01-2421) Sea Surface Temperature reconstruction (Oba *et al.*, 2006; remodelled onto Marine20 timescale), j) 30°N June Insolation (Laskar *et al.*, 2004). Arrows indicate dataset interpretation. Dashed lines approximately align climatic transitions. Abbreviations: Hol = Holocene, YD = Younger Dryas, BA = Bølling–Allerød, H1 = Heinrich Event 1, LGM = Last Glacial Maximum, EAWM = East Asian Winter Monsoon, EASM = East Asian Summer Monsoon, ACR = Antarctic Cold Reversal. Alignment of non-IntCal20/Marine20 timescales was performed as follows: the GRIP $\delta^{18}O_{ice}$ dataset was converted from the GICC05 timescale to the U-Th timescale using the transfer functions of Adolphi and Muscheler (2015) and Adolphi *et al.* (2018). The WD2014 timescale and the U-Th timescale are compatible at the resolution presented here, with a minimal offset at the Holocene onset (Sigl *et al.*, 2016) and an offset of 225 years in the LGM (Sinnl *et al.*, 2023), which has a negligible effect on alignment due to the gradual nature of the changes observed in the WAIS $\delta^{18}O$ record. The U-Th and IntCal20 timescales are compatible because IntCal20, beyond the tree ring limit (circa 13,900 cal BP) is dominated by the Hulu Cave U-Th timescale (Reimer *et al.*, 2020).

Discussion

Our results provide novel insights into the evolution of the EAWM and EASM during TI, alongside their driving mechanisms and teleconnections to other regional climate systems. The gradual decrease in EAWM strength and overall increase in EASM strength in Japan strongly support increasing Northern Hemisphere insolation (driven by Milankovitch cycles) as the primary drivers of EAM evolution (Cheng *et al.*, 2016; Mohtadi *et al.*, 2016; Zhang *et al.*, 2019). However, this common orbital driver breaks down as a result of different responses of each seasonal mode to submillennial temperature fluctuations in either hemisphere and it becomes necessary to evoke alternative mechanisms to rationalise these decoupled (rather than inversely related) seasonal behaviours.

EAWM evolution in Japan appears unaffected by stades in either hemisphere, however other records from Continental Asia (e.g., Lake Huguang Maar (Yancheva *et al.*, 2007)) exhibit significant North Atlantic character (i.e., a BA-YD structure). Despite high quality EAWM records being relatively sparse for this interval, we do not dispute the evidence for a North Atlantic-EAWM teleconnection during TI, and suggest that EAWM wind strength increased (decreased) during stades (interstades) in the North Atlantic, driven by Northern Hemisphere cooling (warming) and an intensified (weakened) Siberian High as previously suggested (Nakagawa *et al.*, 2006). Indeed, the pattern of winter temperatures at Lake Suigetsu provides evidence for the impact of North Atlantic temperatures on the Eurasian airmass (Nakagawa *et al.*, 2021). However, as a consequence of the

interaction of the EAWM winds with the Sea of Japan, the decrease in EAWM strength here was gradual (Fig. 3d). Specifically, we suggest that any response to North Atlantic stade-interstade fluctuations was obscured from our reconstruction by a smoothed, low amplitude response of winter Sea of Japan SSTs to insolation (Wu *et al.*, 2020) and greater inertia in the oceanic domain compared to the terrestrial. Furthermore, we are able to clarify that the previously evidenced bi-partite Late Glacial Stade at Lake Suigetsu (Schlolaut *et al.*, 2017) was not associated with any shifts in EAWM precipitation; whilst there is a 300-year period of lower $\delta^{18}O_{diatom}$ values within this interval (between 12,284 and 12,093 cal BP; Fig. 3d), this fluctuation is not substantially different from other multi-centennial oscillations seen in the profile. However, it remains possible that there was a bipartite pattern in EAWM wind strength. An Antarctica-EAWM teleconnection was precluded by local EAWM moisture transport, the isolation of the Sea of Japan, and the blocking of Pacific Ocean signals by the monsoon front, all of which limited the influence of interhemispheric teleconnections.

Conversely, evidence from Lake Suigetsu supports a response of the EASM to stadial conditions in the southern hemisphere (specifically the ACR) post-16,000 cal BP (Fig. 3f). Previous studies which have noted a relationship between EASM strength and Antarctic temperatures have evoked the bipolar seesaw and migration of the ITCZ as a mechanism to explain this connection (Han *et al.*, 2016; Zhang *et al.*, 2016). Whilst this would facilitate an inverse correlation between EASM strength in Japan and the ACR, it would also suggest that equivalent shifts in the position of the ITCZ caused by North Atlantic behaviours could affect EASM strength, and we do not see evidence of such a relationship in our records. Instead, we suggest that the Antarctic-EASM teleconnection during TI resulted from Antarctic cooling (warming), which caused coupled atmospheric-ocean circulation changes that resulted in warming (cooling) in the Western Pacific Warm Pool, enhanced (decreased) evaporation and a strengthened (weakened) Western Pacific Subtropical High, which caused a stronger (weaker) EASM (Wang and Fan, 2005; Xu *et al.*, 2020).

The coexistence of a North Atlantic teleconnection to summer temperature and an Antarctic teleconnection to summer (EASM) precipitation at Lake Suigetsu is reconcilable by noting that temperature is much more likely to exhibit patterns common to the same hemisphere, whereas the relationship of the EASM to Pacific Ocean behaviours facilitates the influence of the polar Southern Hemisphere on precipitation. Indeed, our observations of EASM strength at Lake Suigetsu, combined with the pollen-derived summer temperature record, support a "Southern Hemisphere lead" to stade/interstade fluctuations during TI; changes in EASM strength led changes in summer temperature because the former was driven by Antarctic processes and the latter by North Atlantic behaviours.

Our observations of EASM behaviour in Japan directly contradict those of the Chinese cave composite, which supports an EASM response to North Atlantic stade-interstade fluctuations and not Antarctic ones (Fig. 3b; Cheng *et al.*, 2016). Because all of the caves included in the composite (Hulu, Sanbao and Dongge) and Lake Suigetsu are located south of the monsoon front during the summer (and hence under the influence of the Pacific air mass; Nakagawa *et al.*, 2006), differences cannot be resolved by the blocking of teleconnections by the monsoon front, as previously suggested (Yoshida and Takeuti, 2009), and instead must be determined by a different geoclimatic boundary. One possible mechanism involves the overprinting of Antarctic signals in Continental Asia by the partitioning of precipitation between the EASM and post-EASM stages (jet-transition hypothesis; Zhang *et al.*, 2018). This phenomenon is linked to the prevailing climatic conditions in the North Atlantic by the timing of the pre-summer northwards shift of the westerly jet and would have caused drier (wetter) conditions in central China during stades (interstades) in the North Atlantic For this to not impact on EASM evolution in Japan, the effect of this partitioning must have been spatially restricted to the continent, or limited to latitudes at, or lower than, the southernmost position of the westerly jet (Lake Suigetsu is located to the north of this position and Hulu, Dongge and Sanbao Cave to the south (Nakagawa *et al.*, 2021)). An alternative explanation is that the

441 speleothem records contain an unresolved temperature-controlled component (demonstrated by
442 their close relationship to the pollen-reconstructed temperature at Lake Suigetsu; both show a
443 remote North Atlantic influence) which obscured the Antarctic signal in favour of a North Atlantic
444 one. Regardless, we posit that the location of Japan at a higher latitude, adjacent to the Pacific
445 Ocean and geographically separated from the rest of East Asia facilitated the preservation of Pacific
446 (and hence Antarctic) signals in our record of EASM behaviour at Lake Suigetsu. Whilst this
447 Antarctica-Japan teleconnection has not been observed in other EASM reconstructions (Wang *et al.*,
448 1999; Ishiwatari *et al.*, 2009; Hayashi *et al.*, 2010), this is likely due to differences in proxy system
449 and a direct relationship between the isotope composition of precipitation and EAM evolution.
450 However, prior to ~16,000 cal BP, EASM strength in Japan and Antarctic temperatures were
451 decoupled. We suggest that the establishment of this teleconnection was as a consequence of the
452 northwards repositioning of the westerly jet (relative to the Himalayas), a phenomenon previously
453 used to explain the onset of the Late Glacial Interstade (BA-equivalent; 15,000 cal BP) at Lake
454 Suigetsu (Nakagawa *et al.*, 2021). Not only did this northwards shift of the westerly jet allow warm
455 Pacific air to reach Japan, it also moved the EAM front to the north of Lake Suigetsu during boreal
456 summer (because the position of the westerly jet also modulates the seasonal positioning of the
457 EAM front), having been situated permanently (year-round) to the south during the LGM (Chiang *et*
458 *al.*, 2015; Nakagawa *et al.*, 2021). This would allow the EASM to propagate to Japan and connect
459 summer precipitation to the aforementioned components of the Pacific atmosphere-oceanic
460 circulation (and hence the southern hemisphere). There were no abrupt shifts in the $\delta^2H_{C30acid}$ values
461 at the onset of the Late Glacial Interstade (15,000 cal BP) to reflect this expansion of EASM operation
462 to include Japan; however, prior to 16,000 cal BP the $\delta^2H_{C30acid}$ values were highly variable and
463 structurally distinctive from WAIS Divide $\delta^{18}O_{ice}$. Hence, we suggest that this Antarctic-Japan
464 teleconnection was established at 16,000 cal BP, facilitated in the 16,000-15,000 cal BP period by
465 intermittent northward migrations of the westerly jet and exposure of Japan to the Pacific airmass

during summer (captured by our centennial sampling resolution), and then continued post-15,000 cal BP when the EAM front was situated permanently to the north of Lake Suigetsu during summer.

It follows that prior to the establishment of this teleconnection, precipitation falling during summer in Japan would not technically be equivalent to the EASM (because it would originate and transit north of the EASM front), and instead would reflect local transport of precipitation under the influence of the continental airmass (possibly following a similar south-east to north-west trajectory due to pressure gradients, but with a significantly reduced transport distance). The highly variable behaviour of the $\delta^2H_{C30acid}$ values (and hence the $\delta^2H_{C16acid}$ values) between 22,000 and 16,000 cal BP may have been caused by the lack of constant, regional driver of summer precipitation (i.e., the EASM) in contrast to the $\delta^{18}O_{diatom}$ values, which were weighted towards the (enduring) EAWM. These fluctuations in the δ^2H_{acid} values could be driven by a number of factors, including precipitation amount, changing relative humidity, shifts in precipitation source and variable SSTs (particularly between 22,000 and 21,000 cal BP (Oba *et al.*, 2006)). Another possible component of this signal is summer meltwater (which could have caused large negative excursions in the $\delta^2H_{C30acid}$ values, such as those observed between ~19,000 and 18,000 cal BP). The significant expansion of the EASM system at 16,000 cal BP has critical implications for other records from the region, particularly those derived from more northerly latitudes, where the influence of the westerly jet migration is more pronounced (Nakagawa et al, 2021). Careful consideration of the location of the monsoon front at this time is vital for robust interpretation of proxy changes and whether they indeed represent EASM evolution or, rather, non-monsoonal summer precipitation.

In conclusion, our findings provide centennial-scale reconstructions which highlight the distinctive seasonal behaviours of the EAM during TI, as well as novel insights into the spatially- and temporally- constrained teleconnections acting on the climate of the EAM region during this interval. Our records are unique in their reconstruction of both seasonal EAM modes in Japan from a single

archive. These results may begin to explain the observed heterogeneity between site-specific reconstructions of EAM behaviour during deglaciation.

Methods

Core Materials

Materials for this study were subsampled from the SG12 core, which was taken from the centre of Lake Suigetsu (35° 35' 08"N, 135° 52' 56"E) and spans a total composite depth of 41.8 m (from the present day to 56,100 cal BP). The core consists of a series of overlapping ~90 cm sections from four boreholes. SG12 is a direct stratigraphic copy of the SG06 core (Nakagawa *et al.*, 2012) due to the proximity of the SG12 and SG06 coring locations (the first borehole of each coring campaign was made within 15 m of each other, and both at a water depth of 34 m). As with the temporally equivalent sediments from the SG06 core, the SG12 sediment is varved throughout and represents continuous sedimentation (Schlolaut *et al.*, 2018). Chronological control for the SG12 cores is given by correlation to the SG06 cores via distinct visible marker layers. The SG06 chronology (Bronk Ramsey *et al.*, 2020; Staff *et al.*, in review) is based on >800 radiocarbon dates for the past ~50 ka BP (Staff *et al.*, 2011; Bronk Ramsey *et al.*, 2020), thin section microscopic varve counts (Schlolaut *et al.*, 2018) and tephra tie points (McLean *et al.*, 2018); all ages are presented on the IntCal20 timescale (Reimer *et al.*, 2020).

Subsamples of the SG12 core for this study were taken from 1.2 cm-wide LL-channels (Nakagawa *et al.*, 2012) from the longitudinally cut core across the composite depth (ver. 27 December 2022) range of 1274.8 – 2119.4 cm (9980 ± 30 cal BP to 22,040 ± 38 cal BP). This time period was selected to encompass the maximum range of the existing Lake Suigetsu pollen-derived temperature reconstruction for TI. The LL-channels were cut to produce contiguous (continuous adjacent) subsamples each containing 100 integrated years of sedimentation (based on the SG06 2012 timescale). Sample ages were subsequently converted to the IntCal20 timescale. A contiguous

integrated sampling approach was taken to avoid subsampling time periods associated with peaks or troughs of multidecadal cycles, superimposed on the multicentennial and multimillennial scale transitions of interest (Nakagawa *et al.*, 2021). The sampling interval of ~100 years was selected to facilitate the detection of finer resolution variability within the key climatic transitions of the period. The (minimal) core expansion during storage was linearly modelled and accounted for by comparing the difference in event layer depth at the time of subsampling to high resolution photographs taken immediately after core extraction. Event layers (floods, turbidites and tephra) were removed during sampling to prevent skewing of the integrated signal by inclusion of a larger quantity of material from a single event. Particular care was taken to avoid contaminating the δ^2H_{acid} samples with modern organic compounds. Surfaces and instruments were regularly cleaned with ethanol.

Each subsample was split into two, with each half designated for $\delta^{18}O_{diatom}$ (n = 120) and δ^2H_{acid} (n = 120) analysis, respectively. The exposed surfaces of one half (for δ^2H_{acid} analysis) were scraped with a clean instrument prior to splitting to remove the outer sediments containing potential contamination from past handling. Wet weights ranged from 1.8 - 10.3 g (subsamples for $\delta^{18}O_{diatom}$ analysis) and 1.1 - 7.1 g (subsamples for δ^2H_{acid} analysis). The largest samples were from the younger end of the section, where the sedimentation rate (and thus depth range equating to ~100 years of integrated time) was high, and the smallest samples were from the older end of the section, where the sedimentation rate was relatively low. All subsamples were frozen and then freeze dried for 24 hours to obtain dry sediment masses before subsequent preparation steps.

$\delta^{18}O_{diatom}$ Analysis

Subsamples for diatom oxygen isotope analysis were prepared following standard procedures (Swann and Snelling, 2023). Specifically, subsamples were disaggregated overnight in 30 % H_2O_2 prior to three successive heavy liquid density separations using sodium polytungstate (SPT) at specific gravities of 2.25 g cm^{-3}, 2.20 g cm^{-3} and 2.15 g cm^{-3}, removing the denser material

each time. The subsamples were subsequently treated with 30 % H_2O_2 at 70 °C for one week to remove any remaining organic material, followed by 5 % HCl for 12 hours to remove carbonates. Subsamples were then filtered using an 80 µm nylon mesh to remove large sponge spicules and large diatoms and freeze dried ready for analysis. As with other studies, further taxa-specific separation was not performed beyond this sieve stage due to the similar size of many diatom taxa present in the samples, rendering physical separation techniques impossible. Qualitative visual purity checks were made using light microscopy at x800 magnification. The $\%Al_2O_3$ for each subsample was quantified using a Malvern Panalytical Epsilon 3 X-Ray Fluorescence (XRF) spectrometer. Due to elevated $\%Al_2O_3$ values in the majority of samples, a Zeiss Sigma 300 VP-FEG Scanning Electron Microscope (SEM) was used to visually identify the source of this aluminium in five samples of varying $\%Al_2O_3$ (Fig. 4). Samples with $\%Al_2O_3$ exceeding 4.2 % (Al/Si = 0.05) showed particulate Al-bearing contamination (most likely a detrital Al-rich silicate, but undetermined due to grain size) which was external to the diatom frustules. These samples (n = 3) were subjected to an additional SPT density separation at 2.15 g cm^{-3} to remove this contamination. Samples with $\%Al_2O_3$ below 4.2 % showed only small amounts (on a sub-micron scale) of this Al-bearing contamination adhered to or trapped within the diatom frustules (Fig. 4). Additional density separations would not remove this contamination due to electrostatic charges adhering the contamination to the frustule, and air pockets within the cylindrical frustules preventing chemical treatment of internal contamination (Brewer *et al.*, 2008), so a mass balancing approach was taken to correct for the effect of this contamination on the $\delta^{18}O_{diatom}$ values (discussed below).

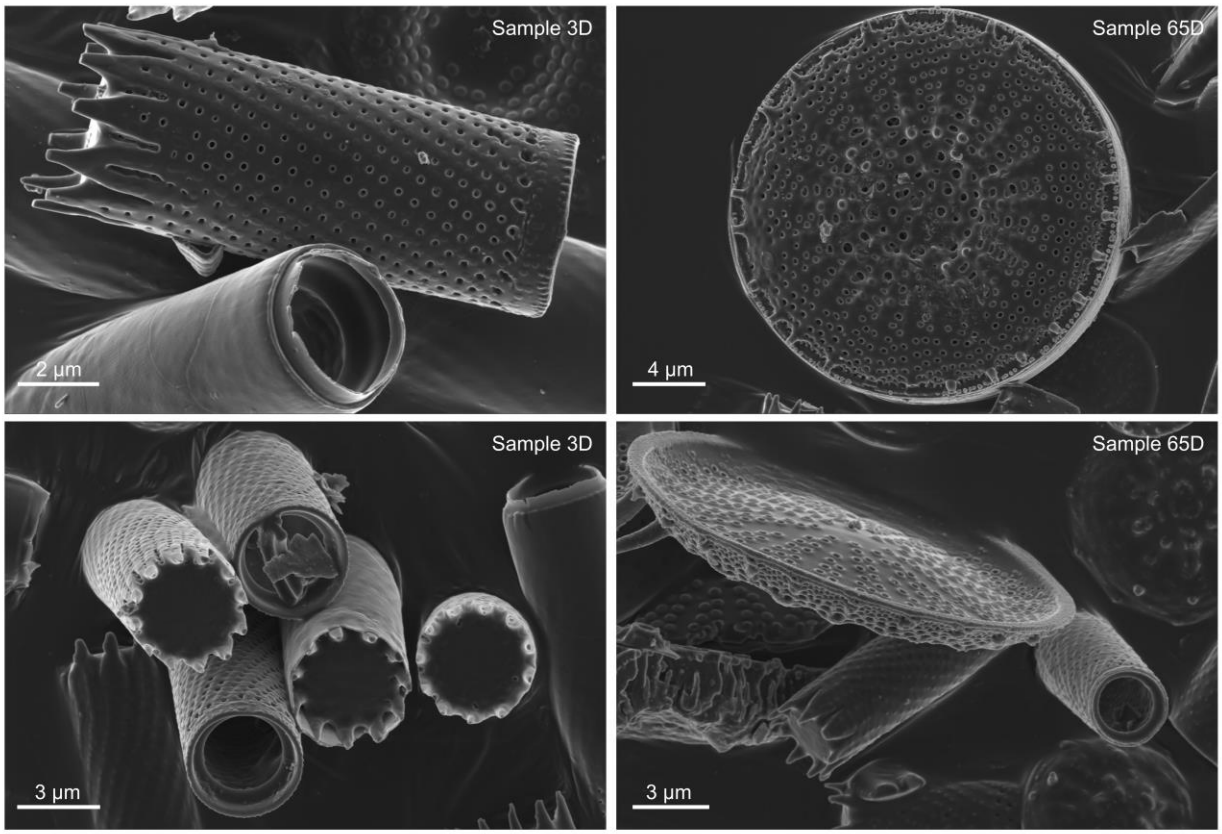

Fig. 4: Diatom SEM Imagery. SEM images for subsample 3D (left) and sample 65D (right) showing Al-bearing contamination adhered to frustules and inside cylindrical *Aulacoseira spp.*, which are representative of the 120 analysed subsamples for $\delta^{18}O_{diatom}$ analysis. Scale bars are indicated on each image.

The purified diatom material (6 – 7 mg subsamples) was subjected to stepwise fluorination in nickel reaction vessels to liberate structural oxygen following Leng and Sloane (2008) at the British Geological Survey (UK). Briefly, this method involved outgassing samples at 250 °C to remove any water in the sample, "pre-fluorination" at 250 °C using a stoichiometric deficiency of BrF_5 to remove the exchangeable hydrous silica layer from the diatom frustules and minimise exchange effects, and then fluorination with BrF_5 overnight at 500 °C. The resulting oxygen gas was cryogenically purified and then converted to CO_2 by exposure to hot platinized graphite (Clayton and Mayeda, 1963). The average gas yield of this process was between 68 and 75 %. In each batch of diatom samples, an in-house laboratory diatomite standard, BFC, with a known value of $\delta^{18}O$ (Chapligin *et al.*, 2011) was also reacted and converted to CO_2 in the same manner following the principle of identical treatment. The oxygen isotope ratio of the diatom subsamples ($\delta^{18}O_{diatom}$) and BFC ($\delta^{18}O_{BFC}$) were measured

relative to a reference CO_2 gas on a Thermo Finnigan MAT 253 dual inlet isotope ratio mass spectrometer. Oxygen isotope ratios were calibrated using a single-point anchoring procedure by analysing CO_2 prepared from an in-house standard (MCS; $\delta^{13}C_{VPDB}$ = −0.7 ‰ and $\delta^{18}O_{VPDB}$ = −9.2 ‰) via reaction with H_3PO_4 (specific gravity = 1.92) at 25°C. All $\delta^{18}O_{VPDB}$ values were converted to the VSMOW scale using Coplen *et al.* (1983) and normalised such that the $\delta^{18}O_{VSMOW}$ of the within-run BFC = +28.9 ‰. The oxygen isotope composition of BFC has been calibrated via inter-laboratory comparison (Chapligin *et al.*, 2011) using the certified international standard NBS 28 ($\delta^{18}O_{VSMOW}$ = +9.57 ‰; Hut, 1987; Gröning *et al.*, 2007). All oxygen isotope data are expressed in standard delta (δ) notation in per mille (‰) deviations relative to VSMOW. External analytical error (1σ) was ±0.13 ‰ for BFC and ±0.33 ‰ for replicate analysis of the diatom samples.

The $\delta^{18}O_{diatom}$ values were corrected for the aforementioned Al-bearing silicate contamination using a geochemical mass balance approach (Mackay *et al.*, 2011; Swann *et al.*, 2018). End member contamination samples for Lake Suigetsu contained 19.45 % Al_2O_3 (from XRF, n = 2), a $\delta^{18}O$ composition of 10.36 ± 0.68 ‰ (1σ range, n = 8) and 48.93 wt% oxygen (from XRF, n = 2). These were prepared from raw materials (n = 2) and the residues of SPT separations from the $\delta^{18}O_{diatom}$ subsamples (n = 6), disaggregated overnight in 30 % H_2O_2 and treated with 30 % H_2O_2 at 70 °C for one week to remove any remaining organic material, followed by 5 % HCl for 12 hours to remove carbonates and 8 % NaOH at 70 °C for 48 hours to remove biogenic silica. Contamination-corrected $\delta^{18}O_{diatom}$ values were modelled using the $\%Al_2O_3$ for each sample, the end member quantities above, and assuming a $\%Al_2O_3$ of pure diatom material of 1.4 % (Al/Si = 0.016), the minimum value measured across the 120 samples. The uncertainty associated with mass-balancing was calculated assuming a normal distribution for data uncertainty and Monte Carlo simulations (10,000 replicates). Errors presented on Fig. 2 and Fig. 3 show the 1σ range of these simulations (mean = ± 0.36 ‰). Of the 120 samples prepared, 113 datapoints are included in the final dataset. Five samples were excluded due to elevated $\%Al_2O_3$ values (>4.2%; Al/Si = 0.05); these produced anomalously high

values during mass balancing, possibly due to atypically large quantities of diatom-bound Al which was unaccounted for by our methods. A further two samples were too small in mass for accurate $\delta^{18}O_{diatom}$ determination via the methods presented above.

δ^2H_{acid} Analysis

Subsamples for δ^2H_{acid} analysis were prepared following the Biomarkers for Environmental and Climate Science (BECS) group standard protocol at the University of Glasgow (UK). The total lipid extract (TLE) was extracted by a Dionex ASE 350 Accelerated Solvent Extractor using dichloromethane and methanol (9:1, v:v) and the TLE dried and weighed. The TLE was then separated into neutral and acid fractions using solid phase extraction through a LC-NH_2 silica gel column. The neutral fraction was eluted using dichloromethane:propan-2-ol solution (1:1, v:v) and the acid fraction using 4 % acetic acid in diethyl ether. The acid fraction was derivatised using 100 µL of 12 % boron trifluoride in methanol in sealed glass vials at 70 °C for 60 minutes. This converted n-alkanoic acids into fatty acid methyl esters (FAMEs) in preparation for analysis. These FAMEs were then cleaned through a silica gel column (35 – 75 µm particle size). Non-FAME material was eluted using hexane and the FAMEs eluted using dichloromethane. Subsamples were prepared in batches of 10 or 11, each with a procedural blank to check for contamination introduced by the stages described above.

Identification of the C_{16}, C_{18}, C_{28} and C_{30} n-alkanoic acids (as FAMEs) was performed on subsample 96B using an Agilent 7890B Gas Chromatograph connected to a 5977A mass spectrometer detector (MSD) with an electron impact (EI) ionisation source (GC-MS). A HP1-MS capillary column was used (60 m length, 0.25 mm internal diameter, 0.25 µm film thickness) with helium carrier gas at a constant flow rate (1.2 mL min^{-1}). The FAMEs were dissolved in DCM (200 µL) and a volume of 1 µL used in a splitless injection. The inlet was kept at 315 °C and the following oven programme used: the oven was held for two minutes at 60 °C and raised to 120 °C at 30 °C min^{-1},

626 then increased to 310 °C at 5 °C min^{-1} and held for 33 minutes. The auxiliary temperature in the
627 transfer line between the GC and MSD was kept constant at 315 °C. The MS source was set to 230
628 and the MS quad set to 160. The detector analysed all compounds between 12- and 65-minute
629 retention time, except for the period between 34 and 39 minutes where flow was redirected to
630 avoid a large phthalate compound peak from entering the detector. Data acquisition was performed
631 in full scan mode at 2.4 scans s^{-1}. Identification of contaminant peaks was also performed using this
632 method. All large contaminant peaks (retention times: ~24.5, ~33 and ~37 minutes) were shown to
633 be phthalate compounds. The largest of these (at ~33 minutes) was present in > 90 % of subsamples,
634 however the others were only present in ~ 10 %. No contaminant peaks obscured the FAME peaks
635 of interest.

636 The concentration of the C_{16}, C_{18}, C_{28} and C_{30} n-alkanoic acids (as FAMEs) in each subsample
637 were measured using an Agilent 7890B Gas Chromatograph fitted with a flame ionisation detector
638 (GC-FID). A Restek Rtx-1 capillary column was used (60 m length, 0.25 mm internal diameter, 0.25
639 µm film thickness) with helium carrier gas at a constant flow rate (1.2 mL min^{-1}). FAMEs were
640 dissolved in DCM (200 µL - 1250 µL; depending on FAME yield) and a volume of 1 µL used in a
641 splitless injection. The inlet was kept at 320 °C and the following oven programme used: the oven
642 was held for two minutes at 60 °C and raised to 120 °C at 30 °C min^{-1}, then increased to 330 °C at 5
643 °C min^{-1} and held for 15 minutes. The FID temperature was set to 250 °C. A chromatogram showing
644 a representative sample with no phthalate peaks is shown in Supplementary Fig. 4. Peak areas were
645 measured, and concentrations calculated from a set of external calibrations using a standard mix of
646 eleven n-alkanes; ten straight-chained (C_{16}, C_{18}, C_{19}, C_{23}, C_{25}, C_{26}, C_{28}, C_{30}, C_{32} and C_{37} n-alkanes) and
647 one branched (squalane). Calibration graphs were made using concentrations of 2.5 µg/mL, 5 µg/mL,
648 and 10 µg/mL. A calibration for the 0 - 25 minute, 25 - 35 minute and 35 - 60 minute retention time
649 intervals were made using the C_{16}, C_{29} and C_{39} homologues in the standard, respectively. An R-
650 squared value of >0.99 was achieved for each calibration. The n-alkanoic acid (as FAME)

concentrations were then normalised to dry sediment weight. Variations in n-alkanoic acid concentrations are shown in Supplementary Fig. 1.

The compound specific hydrogen isotopic composition (δ^2H) of the C_{16}, C_{18}, C_{28} and C_{30} n-alkanoic acids (as FAMEs) were measured using an Agilent 7890B gas chromatography (GC) system connected to an Elementar GC5 furnace and IRMS. The settings of the GC system were identical to those of the GC-FID outlined above with the difference being that the FAMEs were dissolved in between 30 and 120 µL of hexane and the injection volume set to either 1 or 2 µL depending on FAME yield. This ensured that FAMEs were measured as a similar response to the reference H_2 gas. Due to the presence of the largest phthalate compound (retention time ~33 mins) in >90 % of the subsamples, flow was redirected between 1700 s and 1975 s to prevent entry into the IRMS. In 13 subsamples, this was extended to the interval 1400 s to 2100 s to remove the second largest phthalate peak (retention time ~37 minutes). The smallest phthalate peak (retention time ~24.5 minutes) was not larger than the FAME peaks and hence did not require redirection of flow. The furnace temperature was set to 1450 ^oC with an interface temperature of 350 ^oC. Subsamples were measured in duplicate and δ^2H values of each homologue were calculated relative to a calibrated reference H_2 gas. These values were then converted to the VSMOW scale by linear regression to an in-house standard (containing C_{16}, C_{19}, C_{23}, C_{25}, C_{28} and C_{32} straight chained n-alkanes in addition to squalane) calibrated to the standard Indiana n-alkane mixture B5 containing C_{16} to C_{30} n-alkanes. The in-house standard was measured four times prior to each batch, after every eight sample measurements, and in duplicate at the end of each batch. All hydrogen isotope data are expressed in standard delta (δ) notation in per mille (‰) deviations relative to VSMOW. Instrument precision was ±2.53 ‰ based on the standard deviation of all standard measurements. The H_3^+ correction factor ranged from 4.24 to 4.57.

Reliable δ^2H values for all chain lengths across all subsamples was not achieved due to some subsamples exhibiting raised baselines resulting in poorly defined peak areas and inaccurate

676 determination of δ^2H for at least one homologue (affecting 26 subsamples). Raised baselines in
677 some samples predominantly precluded accurate measurement of the aquatic chain lengths,
678 though it was possible to accurately measure the C_{28} and C_{30} homologues in many of the impacted
679 subsamples. Low concentrations affected the repeatability of the measurements of δ^2H_{acid} of at least
680 one homologue in a further 9 subsamples (most commonly C_{16} or C_{18}), hence these values were
681 excluded from the final dataset. The mean precision of the δ^2H_{acid} measurements was ± 2.0 ‰ (1σ
682 range). The resulting dataset has 95 datapoints for the C_{16}, 86 for the C_{18}, 112 for the C_{28} and 108
683 for the C_{30} n-alkanoic acids. Terrestrial and aquatic composites were not generated due to
684 insufficiently strong statistical relationships between the $\delta^2H_{C28acid}$ and $\delta^2H_{C30acid}$ values, and the
685 $\delta^2H_{C16acid}$ and $\delta^2H_{C18acid}$ values, although there was som visual correlation between the two pairs.
686 Values were corrected for the methylation process (which removes the exchangeable carboxylic
687 acid hydrogen from each molecule and replaces it with a methyl group with three hydrogens)
688 (Chivall *et al.*, 2012). GC-IRMS measurements of (Z)-hexadec-9-enoic acid (δ^2H = -154.02 ‰) and
689 methyl (Z)-hexadec-9-enoate (δ^2H = -143.13 ‰) were made to calculate the δ^2H value of a single
690 methanol-derived methyl hydrogen (δ^2H = -37.86 ‰), and a mass balance scheme (Chivall *et al.*,
691 2012) applied to correct the measured FAME δ^2H values to n-alkanoic acid values (excluding the
692 exchangeable hydrogen on the carboxylic acid group).
693
694 **Acknowledgements and Funding**

695 The authors would like to thank the following for their contributions: Mark Wildman
696 (microscope access), Alicja Lacinska (SEM imagery) and Mohammed Ali Salik (δ^2H_{acid} analysis). C.L.
697 Rex was supported by the Natural Environment Research Council IAPETUS2 Doctoral Training
698 Partnership. Diatom isotope analysis was supported by the National Environmental Isotope Facility
699 grant 2308.0920. The authors declare no competing interests.
700

Data Availability

Accompanying data can be found at http://doi.org/10.5525/gla.researchdata.1439.

Supplementary Information

Supplementary Discussion 1

The total lipid extract (TLE) exhibited low values in the early part of the section (~2 mg/g) before increasing gradually from ~15,500 cal BP (Supplementary Fig. 1). Values were then high (~6 mg/g) and fluctuating. This follows the pattern of sediment total organic carbon (TOC) during this period (Tyler *et al.*, 2010). Aquatic n-alkanoic acid concentrations did not show this long-term increasing trend, and the concentration profiles for the C_{16} and C_{18} n-alkanoic acids showed centennial-scale fluctuations throughout (Supplementary Fig. 1). Conversely, the terrestrial n-alkanoic acid concentrations were higher in the latter part of the section; the concentration of the C_{28} n-alkanoic acid showed a greater increase than the C_{30}, but also exhibited larger fluctuations (Supplementary Fig. 1). Throughout, the terrestrial n-alkanoic acid concentrations were generally higher than those of the aquatic n-alkanoic acids, aside from in a small number of samples. The close relationship between the terrestrial n-alkanoic acid concentrations and the TLE concentrations suggests that the terrestrial component was driving the observed TLE increase (allowing for the un-resolved non-acid fractions which also contribute but were not measured). The gradual increase in TLE, TOC and terrestrial n-alkanoic acid concentration was similar in character to the changes in EAWM and EASM strength and very different from the temperature reconstruction for the site (Main Text), suggesting that they were driven by precipitation changes rather than temperature changes. None of these variables show ACR-type inversions, however the seasonality of these variables suggests a relationship to the EASM is more likely than a link to the EAWM, despite the EAWM showing more gradual changes during this interval. Diatom frustule concentration also increased through the section (Supplementary Fig. 1), but the shift to higher values initiated ~500

cal BP later (~15,000 cal BP) and more abruptly than the TLE concentration. Hence, whilst an overall resemblance between frustule concentration and TOC can be argued, there was some decoupling of these variables between ~16,000 and ~15,000 cal BP. The sudden increase in diatom frustule concentration at ~15,000 cal BP was likely driven by temperature changes, in light of the abruptness of this shift and the coincident timing with the onset of the Late Glacial Interstade (Main Text). *Aulacoseira* dominated the diatom assemblage counts, most notably at 21,500 cal BP, 20,000 cal BP and between 15,000 and 12,000 cal BP (Supplementary Fig. 1). Spikes of *Naviculoid* and benthic taxa were observed at 21,000 cal BP. Between 20,000 and 15,000 cal BP there were greater proportions of *Stephanodiscus*, *Naviculoid* and benthic taxa relative to *Aulacoseira*, and similarly a period of increased *Asterionella* between 12,000 and 10,000 cal BP.

751 ***Supplementary Figure 1***

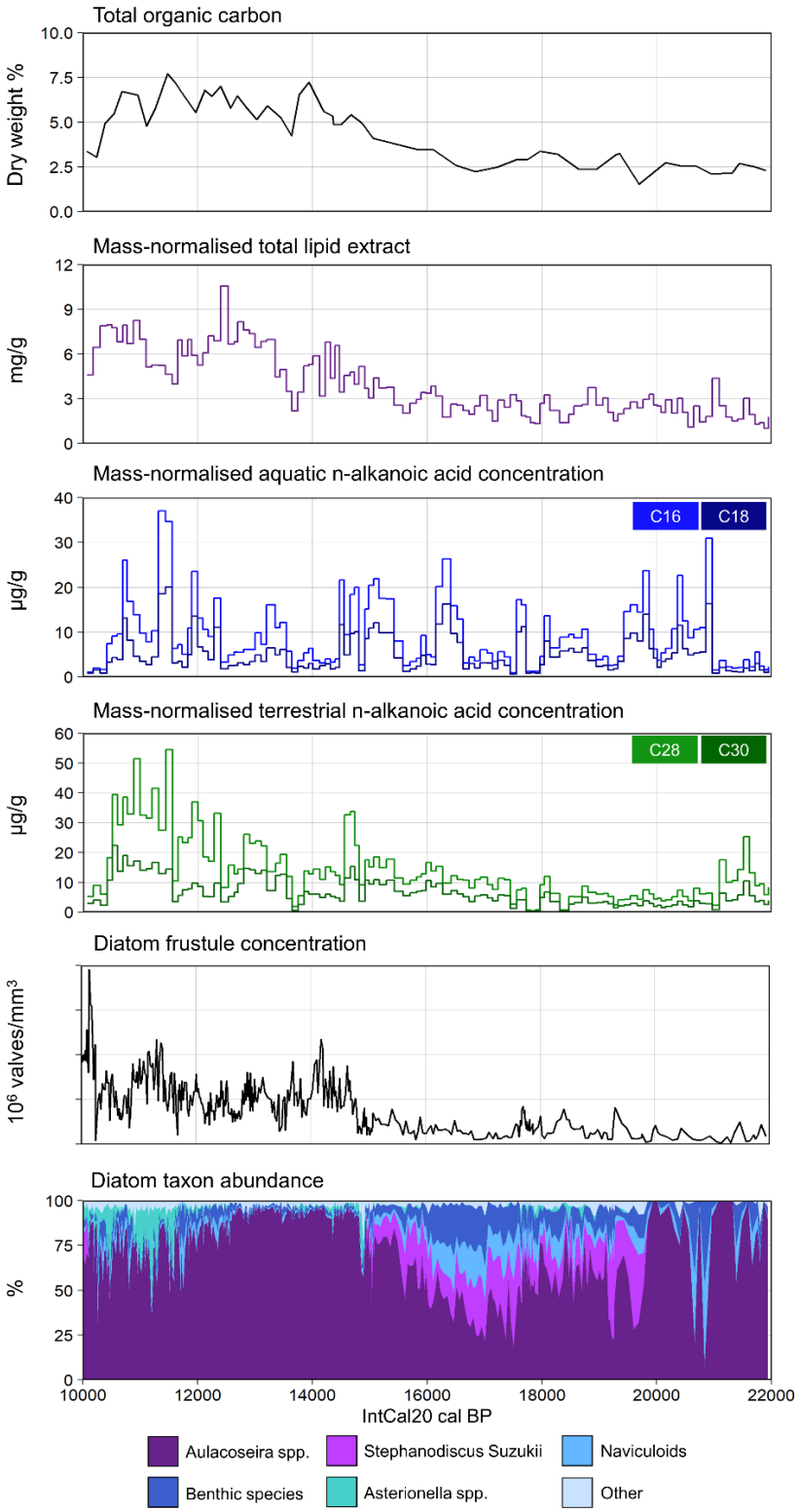

752

753 **Proxy weights, abundances and concentrations.** Variations in total organic carbon (TOC; Tyler *et al.*, 2010),
754 mass-normalised total lipid extract (TLE), mass normalised n-alkanoic acid concentrations (aquatic (C_{16} and
755 C_{18}) and terrestrial (C_{28} and C_{30})), diatom frustule concentration (Saito-Kato *et al.*, unpub) and diatom taxa
756 abundance (Saito-Kato *et al.*, unpub) during TI in the Lake Suigetsu sediment cores.

757

Supplementary Figure 2

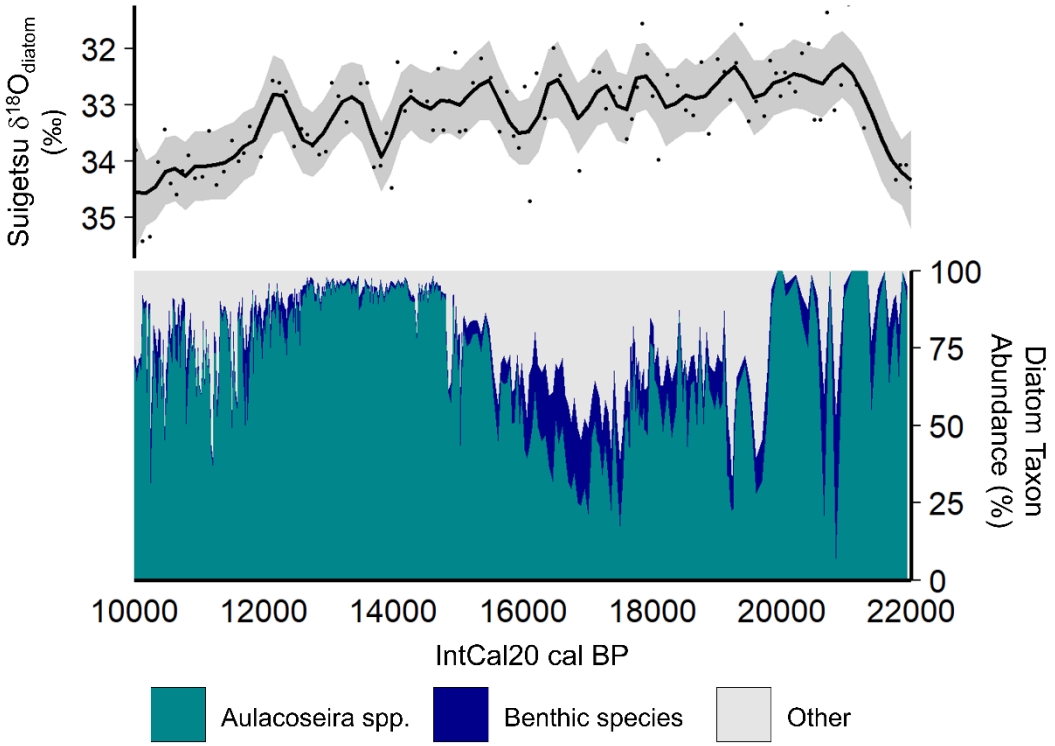

Comparison of Lake Suigetsu $\delta^{18}O_{diatom}$ and Lake Suigetsu diatom taxonomic counts. Diatom taxonomic counts show varying abundances of seasonally assigned genera (*Aulacoseira* and *Encyonema*, a benthic species) versus other taxa. Intervals associated with high *%Aulacoseira* are interpreted as a proxy of EAWM strength. The data presented here supports EAWM weakening during Termination I.

Supplementary Discussion 2

By considering the numerical difference between the $\delta^2H_{C30acid}$ and $\delta^2H_{C16acid}$ values (Supplementary Fig. 3), it is possible to semi-quantify the relative influence of the EAWM and EASM on the $\delta^2H_{C16acid}$ values (which reflects a combination of the $\delta^2H_{precipitation}$ of both seasons; Main Text). Whilst traditionally used to consider the effect of evaporation on the aquatic δ^2H signal (because the terrestrial δ^2H is not affected by lake evaporation, unlike aquatic δ^2H), under the circumstances presented here (and expanded upon in the main text), we interpret this measure to represent the balance between EAWM and EASM influence, based on the inference that the $\delta^2H_{C16acid}$ values represent a seasonal mix, and the $\delta^2H_{C30acid}$ values as seasonally constrained to summer. Following this logic, the numerical difference between these measures indicates increasing EASM influence on

aquatic δ^2H during TI (Supplementary Fig. 3); larger values indicate greater EASM influence, and smaller values indicate greater EAWM influence (based on the assumption that EAWM $\delta^2H_{precipitation}$ is higher than EASM $\delta^2H_{precipitation}$). However, it is inappropriate to apply this interpretation to the ~19,000 – 18,000 cal BP interval, where there was a significant amount of scatter in the $\delta^2H_{C30acid}$ values (discussed in the main text). A reduction in lag time with warming temperatures remains a component of this signal.

Supplementary Figure 3

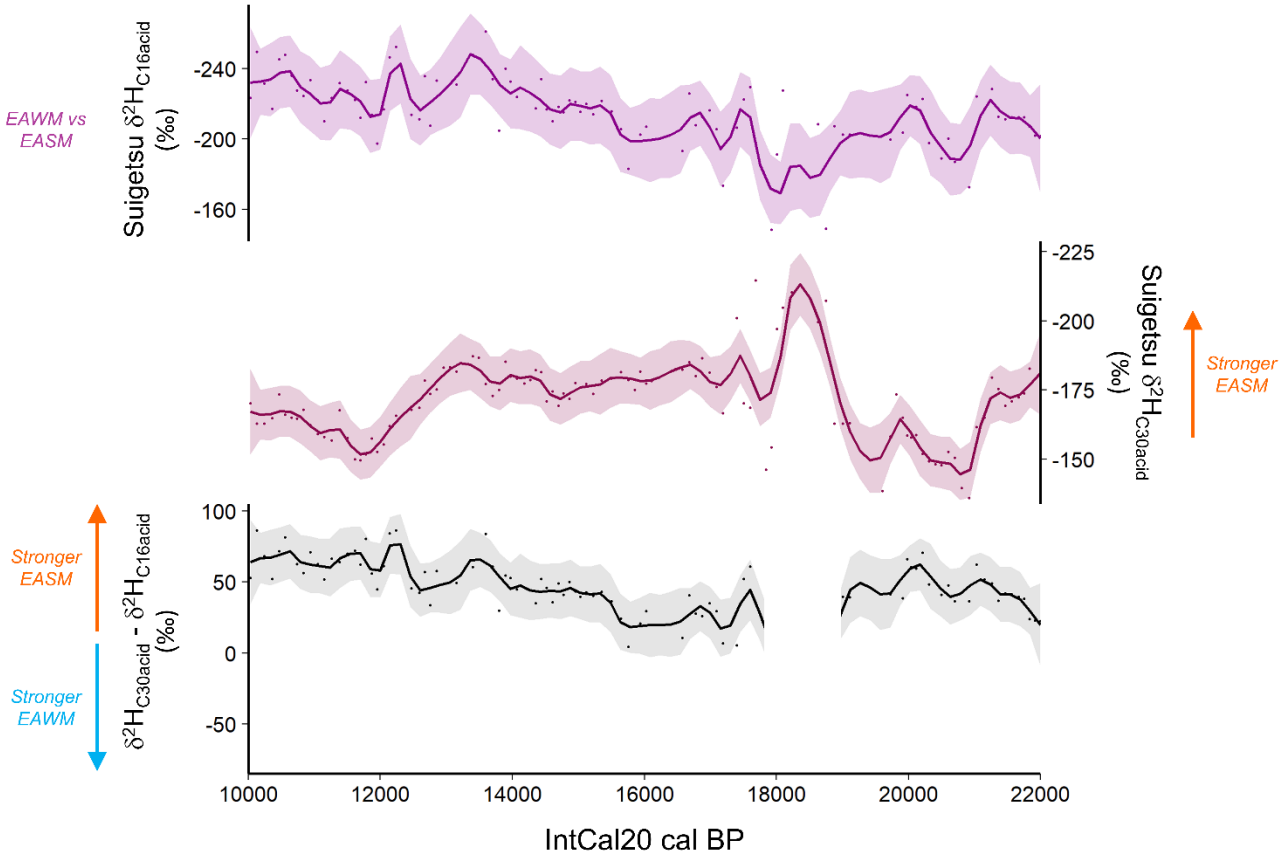

Changing EASM influence on δ^2H_{acid} at Lake Suigetsu. Comparison of Lake Suigetsu $\delta^2H_{C16acid}$, $\delta^2H_{C30acid}$, and the numerical difference between these quantities during TI in the Lake Suigetsu sediment cores. $\delta^2H_{C30acid}$ – $\delta^2H_{C16acid}$ is interpreted as an indicator of EASM versus EAWM influence, with a component of a reduced lag time with warming temperatures.

Supplementary Figure 4

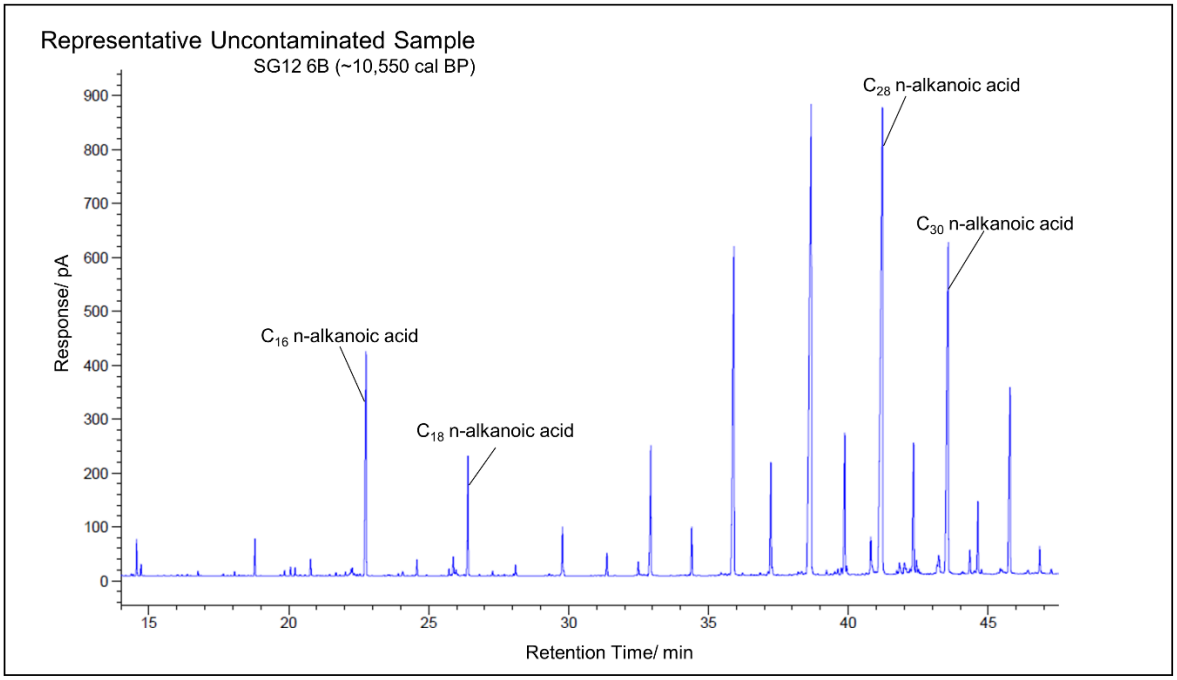

Chromatogram of the n-alkanoic acid fraction of Sample 6B. GC-FID Chromatogram of a representative uncontaminated sample showing clear, symmetrical peaks of interest with a flat chromatogram baseline, strong even-over-odd preference, and dominant terrestrial chain lengths. All n-alkanoic acids were measured as FAMEs.

References

Adolphi, F. & Muscheler, R. Synchronizing the Greenland ice core and radiocarbon timescales over the Holocene – Bayesian wiggle-matching of cosmogenic radionuclide records. *Clim. Past* **12**, 15–30 (2016).

Adolphi, F. *et al.* Connecting the Greenland ice-core and U / Th timescales via cosmogenic radionuclides: testing the synchroneity of Dansgaard–Oeschger events. *Clim. Past* **14**, 1755–1781 (2018).

Amekawa, S. *et al.* Stalagmite evidence for East Asian winter monsoon variability and ^{18}O-depleted surface water in the Japan Sea during the last glacial period. *Prog. Earth Planet. Sci.* **8,** 18 (2021).

808 Brewer, T. S. *et al.* Unravelling contamination signals in biogenic silica oxygen isotope composition:
809 the role of major and trace element geochemistry. *J. Quat. Sci.* **23,** 311–320 (2008).
810 Bronk Ramsey, C. *et al.* Reanalysis of the Atmospheric Radiocarbon Calibration Record from Lake
811 Suigetsu, Japan. *Radiocarbon* **62,** 989–999 (2020).
812 Castañeda, I. S. & Schouten, S. A review of molecular organic proxies for examining modern and
813 ancient lacustrine environments. *Quat. Sci. Rev.* **30,** 2851–2891 (2011).
814 Chapligin, B. *et al.* Inter-laboratory comparison of oxygen isotope compositions from biogenic silica.
815 *Geochim. Cosmochim. Acta* **75,** 7242–7256 (2011).
816 Cheng, H. *et al.* The Asian monsoon over the past 640,000 years and ice age terminations. *Nature*
817 **534,** 640–646 (2016).
818 Chiang, J. C. H. *et al.* Role of seasonal transitions and westerly jets in East Asian paleoclimate. *Quat.*
819 *Sci. Rev.* **108,** 111–129 (2015).
820 Chivall, D., Berstan, R., Bull, I. D. & Evershed, R. P. Isotope effects associated with the preparation
821 and methylation of fatty acids by boron trifluoride in methanol for compound-specific stable
822 hydrogen isotope analysis via gas chromatography/thermal conversion/isotope ratio mass
823 spectrometry. *Rapid Commun. Mass Spectrom.* **26,** 1232–1240 (2012).
824 Chowdary, J. S. *et al.* The Eurasian Jet Streams as Conduits for East Asian Monsoon Variability. *Curr.*
825 *Clim. Chang. Reports* **5,** 233–244 (2019).
826 Clayton, R. N. & Mayeda, T. K. The use of bromine pentafluoride in the extraction of oxygen from
827 oxides and silicates for isotopic analysis. *Geochim. Cosmochim. Acta* **27,** 43–52 (1963).
828 Coplen, T. B., Kendall, C. & Hopple, J. Comparison of stable isotope reference samples. *Nature* **302,**
829 236–238 (1983).
830 Denton, G. H. *et al.* The last glacial termination. *Science* **328,** 1652–1656 (2010).
831 EPICA Community Members. One-to-one coupling of glacial climate variability in Greenland and
832 Antarctica. *Nature* **444,** 195–198 (2006).

Esri (2023). “World Imagery (WGS84)” [basemap]. 1:37,314,123 (panel a), 1:7,851,046 (panel b), 1:530,430 (panel c). Version 12/01/2023. https://www.arcgis.com/home/item.html?id=898f58f2ee824b3c97bae0698563a4b3 (accessed 12/01/2023).

Gallagher, S. J. *et al.* East Asian Monsoon History and Paleoceanography of the Japan Sea Over the Last 460,000 Years. *Paleoceanogr. Paleoclimatology* **33,** 683–702 (2018).

García-Alix, A. *et al.* Paleohydrological dynamics in the Western Mediterranean during the last glacial cycle. *Glob. Planet. Change* **202,** 103527 (2021).

Gröning, M., Dargie, M., Winckler, G. Reference sheet for reference materials: NBS28 & NBS30. *IAEA, Vienna*. 1-5 (2007)

Han, L. Y. *et al.* Potential influence of temperature changes in the Southern Hemisphere on the evolution of the Asian summer monsoon during the last glacial period. *Quat. Int.* **392,** 239–250 (2016).

Hayashi, R., Takahara, H., Hayashida, A. & Takemura, K. Millennial-scale vegetation changes during the last 40,000yr based on a pollen record from Lake Biwa, Japan. *Quat. Res.* **74,** 91–99 (2010).

Herzschuh, U. Palaeo-moisture evolution in monsoonal Central Asia during the last 50,000 years. *Quat. Sci. Rev.* **25,** 163–178 (2006).

Holtvoeth, J. *et al.* The paleolimnologist’s guide to compound-specific stable isotope analysis – An introduction to principles and applications of CSIA for Quaternary lake sediments. *Quat. Sci. Rev.* **207,** 101–133 (2019).

Hut, G. Stable isotope reference samples for geochemical and hydrological investigations (Rep. Consultants Group Meeting, Vienna, 1985). *IAEA, Vienna* (1987)

856 Ishiwatari, R., Negishi, K., Yoshikawa, H. & Yamamoto, S. Glacial-interglacial productivity and
857 environmental changes in Lake Biwa, Japan: A sediment core study of organic carbon,
858 chlorins and biomarkers. *Org. Geochem.* **40,** 520–530 (2009).
859 Johnsen, S. *et al.* The $\delta^{18}O$ record along the Greenland Ice Core Project deep ice core and the
860 problem of possible Eemian climatic instability. *J. Geophys. Res.* **102,** 26,397-26,410 (1997).
861 Kossler, A. *et al.* Onset and termination of the late-glacial climate reversal in the high-resolution
862 diatom and sedimentary records from the annually laminated SG06 core from Lake Suigetsu,
863 Japan. *Palaeogeogr. Palaeoclimatol. Palaeoecol.* **306,** 103–115 (2011).
864 Laskar, J. *et al.* A long-term numerical solution for the insolation quantities of the Earth. *Astron.*
865 *Astrophys.* **428,** 261–285 (2004).
866 Leng, M. J. & Barker, P. A. A review of the oxygen isotope composition of lacustrine diatom silica for
867 palaeoclimate reconstruction. *Earth-Science Rev.* **75,** 5–27 (2006).
868 Leng, M. J. & Marshall, J. D. Palaeoclimate interpretation of stable isotope data from lake sediment
869 archives. *Quat. Sci. Rev.* **23,** 811–831 (2004).
870 Leng, M. J. & Sloane, H. J. Combined oxygen and silicon isotope analysis of biogenic silica. J. Quat.
871 Sci. **23,** 313–319 (2008).
872 Liu, X. *et al.* Centennial-scale East Asian winter monsoon variability within the Younger Dryas.
873 *Palaeogeogr. Palaeoclimatol. Palaeoecol.* **601,** 111101 (2022).
874 Mackay, A. W. *et al.* A reassessment of late glacial - Holocene diatom oxygen isotope record from
875 Lake Baikal using a geochemical mass-balance approach. *J. Quat. Sci.* **26,** 627–634 (2011).
876 McLean, D. *et al.* Integrating the Holocene tephrostratigraphy for East Asia using a high-resolution
877 cryptotephra study from Lake Suigetsu (SG14 core), central Japan. *Quat. Sci. Rev.* **183,** 36–
878 58 (2018).
879 Mohtadi, M., Prange, M. & Steinke, S. Palaeoclimatic insights into forcing and response of monsoon
880 rainfall. *Nature* **533,** 191–199 (2016).

881 Nakagawa, T. *et al.* SG06, a fully continuous and varved sediment core from Lake Suigetsu, Japan:
882 Stratigraphy and potential for improving the radiocarbon calibration model and
883 understanding of late Quaternary climate changes. *Quat. Sci. Rev.* **36,** 164–176 (2012).
884 Nakagawa, T. *et al.* The spatio-temporal structure of the Lateglacial to early Holocene transition
885 reconstructed from the pollen record of Lake Suigetsu and its precise correlation with other
886 key global archives: Implications for palaeoclimatology and archaeology. *Glob. Planet.*
887 *Change* **202,** 103493 (2021).
888 Nakagawa, T., Tarasov, P. E., Kitagawa, H., Yasuda, Y. & Gotanda, K. Seasonally specific responses of
889 the East Asian monsoon to deglacial climate changes. *Geology* **34,** 521–524 (2006).
890 Oba, T. & Murayama, M. Sea-surface temperature and salinity changes in the northwest Pacific since
891 the last glacial maximum. *J. Quat. Sci.* **19,** 335–346 (2004).
892 Oba, T. *et al.* Paleoceanographic change off central Japan since the last 144,000 years based on high-
893 resolution oxygen and carbon isotope records. Glob. Planet. Change **53,** 5–20 (2006).
894 Rasmussen, S. O. *et al.* A stratigraphic framework for abrupt climatic changes during the Last Glacial
895 period based on three synchronized Greenland ice-core records: Refining and extending the
896 INTIMATE event stratigraphy. *Quat. Sci. Rev.* **106,** 14–28 (2014).
897 Reimer, P. J. *et al.* The IntCal20 Northern Hemisphere Radiocarbon Age Calibration Curve (0-55 cal
898 kBP). *Radiocarbon* **62,** 725–757 (2020).
899 Rex, C. L. *et al.* The contemporary stable isotope hydrology of Lake Suigetsu and surrounding
900 catchment (Japan) and its implications for sediment-derived palaeoclimate records. Preprint,
901 EarthArXiv (2023). Available at: https://doi.org/10.31223/X53X2D
902 Sachse, D. *et al.* Molecular Paleohydrology: Interpreting the Hydrogen-Isotopic Composition of Lipid
903 Biomarkers from Photosynthesizing Organisms. *Annu. Rev. Earth Planet. Sci.* **40,** 221–249
904 (2012).

905 Schlolaut, G. *et al.* An automated method for varve interpolation and its application to the Late
906 Glacial chronology from Lake Suigetsu, Japan. *Quat. Geochronol.* **13,** 52–69 (2012).
907 Schlolaut, G. *et al.* An extended and revised Lake Suigetsu varve chronology from ∼50 to ∼10 ka BP
908 based on detailed sediment micro-facies analyses. *Quat. Sci. Rev.* **200,** 351–366 (2018).
909 Schlolaut, G. *et al.* Evidence for a bi-partition of the Younger Dryas Stadial in East Asia associated
910 with inversed climate characteristics compared to Europe. *Sci. Rep.* **7,** 44983 (2017).
911 Sigl, M. *et al.* The WAIS Divide deep ice core WD2014 chronology – Part 2: Annual-layer counting
912 (0–31 ka BP). *Clim. Past* **12**, 769–786 (2016).
913 Sinnl, G. *et al.* Synchronizing ice-core and U/Th timescales in the Last Glacial Maximum using Hulu
914 Cave ^{14}C and new ^{10}Be measurements from Greenland and Antarctica. *Clim. Past* **19**, 1153–
915 1175 (2023).
916 Sone, T. *et al.* Holocene stalagmite oxygen isotopic record from the Japan Sea side of the Japanese
917 Islands, as a new proxy of the East Asian winter monsoon. *Quat. Sci. Rev.* **75,** 150–160 (2013).
918 Staff, R. A. *et al.* New ^{14}C determinations from Lake Suigetsu, Japan: 12,000 to 0 cal BP. *Radiocarbon*
919 **53,** 511–528 (2011).
920 Swann, G. & Snelling, A. Isotope sample preparation of diatoms for paleoenvironmental research
921 V.2. *PLoS ONE* **18,** e0281511 (2023).
922 Swann, G. E. A. *et al.* Lake Baikal isotope records of Holocene Central Asian precipitation. *Quat. Sci.*
923 *Rev.* **189,** 210–222 (2018).
924 Tierney, J. E., Torfstein, A. & Bhattacharya, T. Late Quaternary hydroclimate of the Levant: The leaf
925 wax record from the Dead Sea. *Quat. Sci. Rev.* **289,** 107613 (2022).
926 Tyler, J. J. *et al.* Tracking aquatic change using chlorine-specific carbon and nitrogen isotopes: The
927 last glacial-interglacial transition at Lake Suigetsu, Japan. *Geochemistry, Geophys.*
928 *Geosystems* **11,** Q09010 (2010).

van Bree, L. G. J. *et al.* Seasonal variability in the abundance and stable carbon-isotopic composition of lipid biomarkers in suspended particulate matter from a stratified equatorial lake (Lake Chala, Kenya/Tanzania): Implications for the sedimentary record. *Quat. Sci. Rev.* **192**, 208–224 (2018).

van Hardenbroek, M. *et al.* The stable isotope composition of organic and inorganic fossils in lake sediment records: Current understanding, challenges, and future directions. *Quat. Sci. Rev.* **196**, 154–176 (2018).

WAIS Divide Project Members. Onset of deglacial warming in West Antarctica driven by local orbital forcing. *Nature* **500,** 440–444 (2013).

Wang, H. & Fan, K. Central-north China precipitation as reconstructed from the Qing dynasty: Signal of the Antarctic Atmospheric Oscillation. *Geophys. Res. Lett.* **32,** L24705 (2005).

Wang, L. *et al.* East Asian monsoon climate during the Late Pleistocene: High-resolution sediment records from the South China Sea. *Mar. Geol.* **156,** 245–284 (1999).

Wang, L. *et al.* The East Asian winter monsoon over the last 15,000 years: Its links to high-latitudes and tropical climate systems and complex correlation to the summer monsoon. *Quat. Sci. Rev.* **32,** 131–142 (2012).

Wang, Y. J. *et al.* A high-resolution absolute-dated late pleistocene monsoon record from Hulu Cave, China. *Science* **294,** 2345–2348 (2001).

Wen, X., Liu, Z., Wang, S., Cheng, J. & Zhu, J. Correlation and anti-correlation of the East Asian summer and winter monsoons during the last 21,000 years. *Nat. Commun.* **7,** 11999 (2016).

Wu, Y. *et al.* Evolution of the Upper Ocean Stratification in the Japan Sea Since the Last Glacial. *Geophys. Res. Lett.* **47,** e2020GL088255 (2020).

Xu, H. *et al.* Juxtaposition of Western Pacific Subtropical High on Asian Summer Monsoon Shapes Subtropical East Asian Precipitation. *Geophys. Res. Lett.* **47,** e2019GL084705 (2020).

953 Yan, M., Liu, Z. Y., Ning, L. & Liu, J. Holocene EASM-EAWM Relationship Across Different Timescales
954 in CCSM3. *Geophys. Res. Lett.* **47,** e2020GL088451 (2020).
955 Yancheva, G. *et al.* Influence of the intertropical convergence zone on the East Asian monsoon.
956 *Nature* **445,** 74–77 (2007).
957 Yoshida, A. & Takeuti, S. Quantitative reconstruction of palaeoclimate from pollen profiles in
958 northeastern Japan and the timing of a cold reversal event during the Last Termination. *J.*
959 *Quat. Sci.* **24,** 1006–1015 (2009).
960 Yuan, D. *et al.* Timing, Duration, and Transitions of the Last Interglacial Asian Monsoon. *Science* **304,**
961 575–578 (2004).
962 Zhang, H. *et al.* Antarctic link with East Asian summer monsoon variability during the Heinrich
963 Stadial–Bølling interstadial transition. *Earth Planet. Sci. Lett.* **453,** 243–251 (2016).
964 Zhang, H. *et al.* East Asian hydroclimate modulated by the position of the westerlies during
965 Termination I. *Science* **362,** 580–583 (2018).
966 Zhang, H. *et al.* The Asian Summer Monsoon: Teleconnections and Forcing Mechanisms—A Review
967 from Chinese Speleothem δ18O Records. *Quaternary* **2,** 26 (2019).